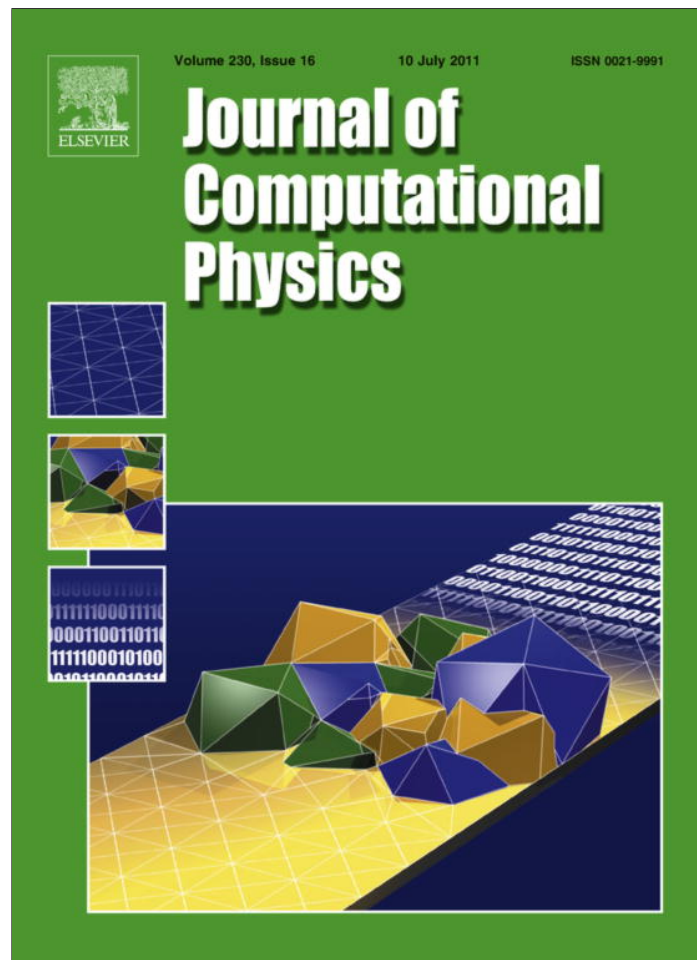


Provided for non-commercial research and education use.
Not for reproduction, distribution or commercial use.



This article appeared in a journal published by Elsevier. The attached copy is furnished to the author for internal non-commercial research and education use, including for instruction at the authors institution and sharing with colleagues.

Other uses, including reproduction and distribution, or selling or licensing copies, or posting to personal, institutional or third party websites are prohibited.

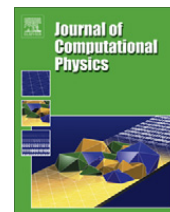
In most cases authors are permitted to post their version of the article (e.g. in Word or Tex form) to their personal website or institutional repository. Authors requiring further information regarding Elsevier's archiving and manuscript policies are encouraged to visit:

<http://www.elsevier.com/copyright>



Contents lists available at ScienceDirect

Journal of Computational Physics

journal homepage: www.elsevier.com/locate/jcp

Effects of discontinuous magnetic permeability on magnetodynamic problems

J.-L. Guermond^{a,*,1}, J. Léorat^b, F. Luddens^{a,c}, C. Nore^{c,d,e}, A. Ribeiro^c

^a Department of Mathematics, Texas A&M University 3368 TAMU, College Station, TX 77843-3368, USA

^b Luth, Observatoire de Paris-Meudon, place Janssen, 92195-Meudon, France

^c Laboratoire d'Informatique pour la Mécanique et les Sciences de l'Ingénieur, CNRS, BP 133, 91403 Orsay cedex, France

^d Université Paris Sud 11, Département de Physique, 91405 Orsay cedex, France

^e Institut Universitaire de France, 103, bd Saint-Michel 75005 Paris, France

ARTICLE INFO

Article history:

Received 23 November 2010

Received in revised form 17 April 2011

Accepted 19 April 2011

Available online 28 April 2011

Keywords:

Finite elements

Discontinuous Galerkin

Magnetohydrodynamics

Discontinuous magnetic permeability

Kinematic dynamo action

ABSTRACT

A novel approximation technique using Lagrange finite elements is proposed to solve magneto-dynamics problems involving discontinuous magnetic permeability and non-smooth interfaces. The algorithm is validated on benchmark problems and is used for kinematic studies of the Cadarache von Kármán Sodium 2 (VK2) experimental fluid dynamo.

© 2011 Elsevier Inc. All rights reserved.

1. Introduction

This paper is the third part of a research program whose goal is to develop a solution method for solving the magneto-hydrodynamic equations in heterogeneous axisymmetric domains. The computational domain is assumed to be composed of non-conducting and conducting media. The electromagnetic field is represented by the pair $\mathbf{H} - \phi$, where \mathbf{H} denotes the magnetic field in the conducting region and ϕ denotes the magnetic scalar potential in the non-conducting region. The basic ideas for approximating this class of problems have been introduced in [15]. Lagrange finite elements are used in the median section and variations in the azimuthal direction are approximated with Fourier expansions. The approximation is discontinuous across the interface separating the conducting and the non-conducting domains. This choice allows us to use Lagrange elements. The coupling between the \mathbf{H} and ϕ representations is done by using an Interior Penalty technique [2,3]. The method has been applied in [15] to the Maxwell equations forced by given velocity fields; this is the so-called kinematic dynamo problem. The solution method has been shown to be stable and convergent. In [16], the method has been generalized to the full magnetohydrodynamic (MHD) problems and has been shown to be capable of solving nontrivial nonlinear

* Corresponding author.

E-mail addresses: guermond@math.tamu.edu (J.-L. Guermond), Jacques.Leorat@obspm.fr (J. Léorat), luddens@limsi.fr (F. Luddens), nore@limsi.fr (C. Nore), ribeiro@limsi.fr (A. Ribeiro).

¹ On long leave from LIMSI (CNRS-UPR 3251), BP 133, 91403, Orsay, France. This author is supported in part by the National Science Foundation grants DMS-0713829 and DMS-1015984. This publication is based in part on work supported by Award No. KUS-C1-016-04, made by King Abdullah University of Science and Technology (KAUST).

dynamo problems. The Navier–Stokes/Maxwell coupling together with details on a parallelization technique for the fast Fourier transform (FFT) method are described in [16].

The main restriction of the method introduced in [15,16] is that the magnetic permeability must be smooth in the conducting region. This is a major impediment since magnetic permeability heterogeneity is suspected to play a key role in the confinement of the magnetic field in some dynamo experiments (we refer in particular to the VKS2 (von Kármán Sodium 2) successful dynamo experiment [26]) and thus significantly lowers the dynamo threshold, [19]. The second restriction is that our using Lagrange finite elements and penalizing the divergence of the magnetic induction in L^2 requires all the interfaces to be either smooth or the convexity of the interfaces be oriented towards the non-conducting region. This geometrical restriction is sometimes cumbersome. The objective of the present work is to address the two above issues. We show in the present work that the approximation framework proposed in [15,16] can be generalized to account for magnetic permeability jumps and possible lack of smoothness of the interfaces where the electric conductivity and the magnetic permeability are discontinuous.

The paper is organized as follows. Notation and basic notions regarding the continuous problem are introduced and discussed in Section 2. The finite element approximation is presented in Section 3. In addition to accounting for discontinuous magnetic permeability, the main novelty of the method is condensed in the bilinear form \mathcal{D} in the weak formulation 3.11. The new method is tested numerically on various academic benchmark problems in Section 4. The method is shown therein to be robust with respect to geometric singularities and high magnetic permeability contrasts. The method is finally used in Section 5 to explore various aspects of the VKS2 experiment. Our numerical results confirm the experimental observation that using soft iron components in the VKS2 experiment significantly lowers the dynamo threshold.

2. Setting of the magnetic problem

The purpose of this section is to describe the PDE setting. We focus our attention on the magnetic features of the problem since the main novelty that we are going to introduce with respect to [15,16] consists of accounting for the discontinuities of magnetic permeability field. The Navier–Stokes part of the full MHD problem is thus not considered in this paper.

2.1. The geometric setting

We consider the MHD equations in a bounded axisymmetric domain $\Omega \subset \mathbb{R}^3$ (Ω could be a truncated version of an unbounded domain). The boundary of Ω is denoted by $\Gamma = \partial\Omega$ and is henceforth assumed to be at least Lipschitz continuous. Ω is assumed to be partitioned into a conducting region (subscript c) and an insulating region (subscript v) as follows:

$$\overline{\Omega} = \overline{\Omega_c} \cup \overline{\Omega_v}, \quad \Omega_c \cap \Omega_v = \emptyset. \quad (2.1)$$

Ω_c is referred to as the conducting domain and Ω_v is referred to as the non-conducting domain. The interface between the conducting region and the non-conducting region is given and denoted by

$$\Sigma = \partial\Omega_c \cap \partial\Omega_v. \quad (2.2)$$

The magnetic permeability, μ , is assumed to be axisymmetric and piece-wise smooth over Ω_c . More precisely, we assume that the conducting region, Ω_c , can be partitioned into subregions $\Omega_{c1}, \dots, \Omega_{cN}$ so that the restriction of μ over each subregion, $\Omega_{ci}, i \in \overline{1, N}$, is smooth. In other words,

$$\overline{\Omega_c} = \overline{\Omega_{c1}} \cup \dots \cup \overline{\Omega_{cN}}, \quad \Omega_{ci} \cap \Omega_{cj} = \emptyset, \quad \forall i, j \in \overline{1, N}. \quad (2.3)$$

The interface between all the conducting subregions is also given and denoted by Σ_μ ,

$$\Sigma_\mu = \cup_{i,j \in \overline{1, N}} \overline{\Omega_{ci}} \cap \overline{\Omega_{cj}}. \quad (2.4)$$

The interfaces Σ and Σ_μ are fixed and given; they correspond to changes of material properties and one side of these interfaces is always a non-deformable solid.

To easily refer to boundary conditions, we introduce

$$\Gamma_c = \Gamma \cap \partial\Omega_c, \quad \Gamma_v = \Gamma \cap \partial\Omega_v. \quad (2.5)$$

Note that $\Gamma = \Gamma_v \cup \Gamma_c$. Moreover, we denote by Γ_v^0 the connected component of $\partial\Omega_v$ that contains Γ_v . We assume that $\partial\Omega_v$ has $J+1$ connected components, say

$$\Gamma_v^0, \Gamma_v^1, \dots, \Gamma_v^J. \quad (2.6)$$

Observe that $\Sigma = (\Gamma_v^0 \setminus \Gamma_v) \cup \Gamma_v^1 \cup \dots \cup \Gamma_v^J$

The notation is illustrated in Fig. 1 on two examples. The vertical dashed line represents the symmetry axis. Only the meridional section of each region is shown. The geometry shown in the left panel (a) has $J=2$ (3 conducting torii), and $\Sigma = (\Gamma_v^0 \setminus \Gamma_v) \cup \Gamma_v^1 \cup \Gamma_v^2$. The conducting region is composed of 5 subregions. The geometry shown in the right panel (b) has $J=1$, $\Gamma_v^0 = \Gamma_v$, $\Gamma_c = \emptyset$, and $\Sigma = \Gamma_v^1$. The conducting region is composed of 2 subregions of different electric conductivities and magnetic diffusivities.

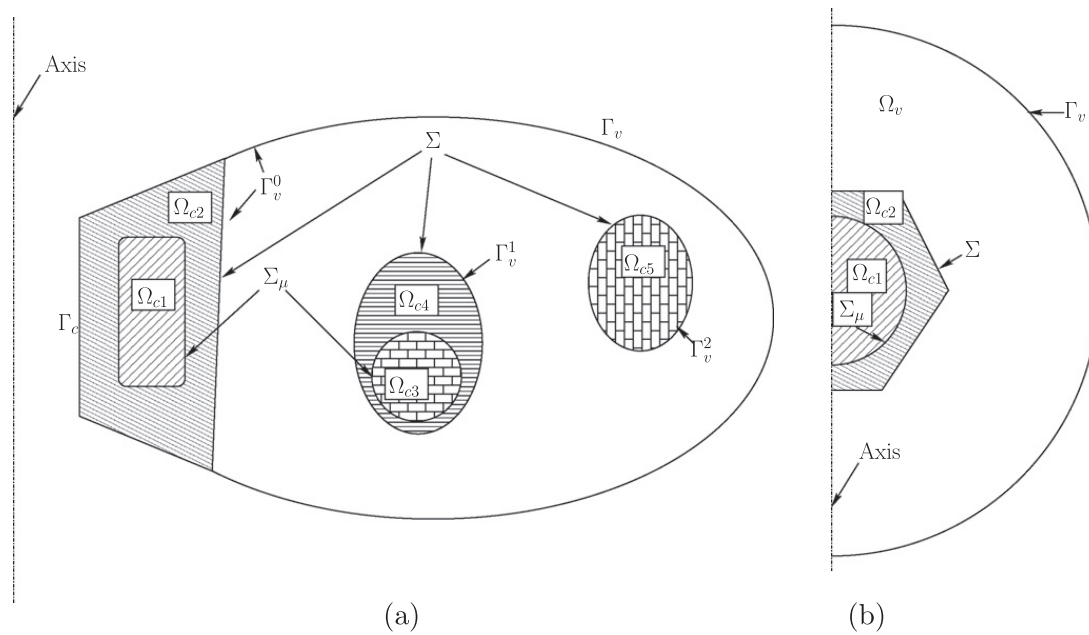


Fig. 1. Examples of computational domains with various boundaries. The left line is the revolution axis. The shaded regions constitute the conducting domain Ω_c , the non-shaded domain is vacuum Ω_v . The dashed subregions may have different electric conductivities and magnetic permeabilities.

2.2. The PDE setting

The conducting region is composed of fluid and solid domains, with conductivity and permeability jumps. The time evolution of the magnetic and electric fields is modeled by the Maxwell equations. To simplify the presentation, we assume in this paper that the velocity field of the fluid and that of the solid moving parts are known and we denote this quantity by $\tilde{\mathbf{u}}$. No notational distinction is made to separate the fluid and the solid regions.

The time evolution of the electromagnetic field is modeled as follows:

$$\begin{cases} \mu \partial_t \mathbf{H} = -\nabla \times \mathbf{E}, & \text{in } \Omega \\ \nabla \times \mathbf{H} = \begin{cases} \sigma(\mathbf{E} + \tilde{\mathbf{u}} \times \mu \mathbf{H}) + \mathbf{j}^s, & \text{in } \Omega_c \\ 0, & \text{in } \Omega_v \end{cases} \\ \nabla \cdot \mathbf{E} = 0, & \text{in } \Omega_v \\ \mathbf{E} \times \mathbf{n}|_\Gamma = \mathbf{a}, \quad \mathbf{H}|_{t=0} = \mathbf{H}_0, & \text{in } \Omega_c \\ \int_{\Gamma_v^i} \mathbf{E} \cdot \mathbf{n} = 0, \quad 1 \leq i \leq J \end{cases} \quad (2.7)$$

where \mathbf{n} is the outward normal on Γ . The independent variables are space and time. The dependent variables are the magnetic field, \mathbf{H} , and the electric field, \mathbf{E} . The physical parameters are the magnetic permeability, μ , and the electric conductivity, σ . The data are \mathbf{H}_0 , \mathbf{a} and \mathbf{j}^s : \mathbf{H}_0 is an initial data; \mathbf{a} is a boundary data; \mathbf{j}^s is an externally imposed distribution of current. The initial magnetic induction field, $\mu \mathbf{H}_0$, is assumed to satisfy the compatibility condition $\nabla \cdot (\mu \mathbf{H}_0) = 0$.

Let \mathcal{U} be the characteristic scale of $\tilde{\mathbf{u}}$ and let c be the speed of light. The MHD approximation consists of assuming that the ratio \mathcal{U}/c is extremely small. This hypothesis leads to neglect the displacement currents $\epsilon \partial_t \mathbf{E}$ in the Ampère–Maxwell equation. Note however that the conditions $\nabla \cdot \mathbf{E}|_{\Omega_v} = 0$ and $\int_{\Gamma_v^i} \mathbf{E} \cdot \mathbf{n} = 0, 1 \leq i \leq J$ are what is left from the Ampère–Maxwell equation when passing to the limit to zero on the ratio \mathcal{U}/c (assuming that the total electrostatic charge in each conducting region is zero). These extra conditions ensure that \mathbf{E} is uniquely defined, i.e., they have no effect on \mathbf{H} . Note finally that the condition $\int_{\Gamma_v^0} \mathbf{E} \cdot \mathbf{n} = 0$ needs not be enforced since it is a consequence of the J other conditions, $\int_{\Gamma_v^i} \mathbf{E} \cdot \mathbf{n} = 0, i = 1, \dots, J$, together with \mathbf{E} being solenoidal. We refer to [5,1] for more details on the asymptotic analysis leading to (2.7).

When σ is uniformly positive over Ω , i.e., $\Omega_c = \Omega$ and $\Omega_v = \emptyset$, an evolution equation for \mathbf{H} can be obtained after eliminating the electric field. This shortcut is no longer possible when Ω_v is non trivial, and determining the complete solution, including the electric field, is no longer straightforward.

We henceforth assume that the conductivity σ is zero in Ω_v and is bounded from below and from above in Ω_c by positive constants. We also assume that the restriction of μ to Ω_v is a smooth function, and that μ is piece-wise smooth on Ω_c , i.e., $\mu|_{\Omega_{c_i}}$ is smooth for all $i = 1, \dots, N$.

2.3. Non-dimensionalization of the equations

We now non-dimensionalize 2.7. We denote by \mathcal{L} and \mathcal{U} reference length and velocity scales, respectively. Our basic assumption is that $\mathcal{U} \ll c$, where c is the speed of light. The reference (advective) time scale is $\mathcal{T} := \mathcal{L}/\mathcal{U}$. The fluid density

is assumed to be a constant ρ . The reference magnetic permeability and electric conductivity are denoted by μ_0 and σ_0 , respectively. We choose the reference scale for the magnetic field to be so that the reference Alfvén speed is one, i.e., $\mathcal{H} := \mathcal{U}\sqrt{\rho/\mu_0}$. The reference scale for the electric field is set to be $\mathcal{E} := \mu_0\mathcal{H}\mathcal{U}$. The source current \mathbf{j}^s and the data \mathbf{H}_0, \mathbf{a} are non-dimensionalized by $\mathcal{H}\mathcal{L}^{-1}, \mathcal{H}$ and \mathcal{H} , respectively. This leaves one non-dimensional parameter which we refer to as the magnetic Reynolds number, R_m , and which is defined as follows:

$$R_m := \mathcal{U}\mathcal{L}\sigma_0\mu_0. \tag{2.8}$$

Henceforth we abuse the notation by using the same symbols for the non-dimensional and the corresponding dimensional quantities. The non-dimensional set of equations is re-written as follows:

$$\begin{cases} \mu\partial_t\mathbf{H} = -\nabla \times \mathbf{E}, & \text{in } \Omega \\ \nabla \times \mathbf{H} = \begin{cases} R_m\sigma(\mathbf{E} + \tilde{\mathbf{u}} \times \mu\mathbf{H}) + \mathbf{j}^s, & \text{in } \Omega_c \\ 0, & \text{in } \Omega_v \end{cases} \\ \nabla \cdot \mathbf{E} = 0, & \text{in } \Omega_v \\ \mathbf{E} \times \mathbf{n}|_{\Gamma} = \mathbf{a}, \quad \mathbf{H}|_{t=0} = \mathbf{H}_0, & \text{in } \Omega_c \\ \int_{\Gamma^i} \mathbf{E} \cdot \mathbf{n} = 0, \quad 1 \leq i \leq J, \end{cases} \tag{2.9}$$

where σ and μ are the relative conductivity and permeability, respectively.

2.4. Introduction of ϕ and elimination of \mathbf{E}

In addition to the above geometrical hypotheses on Ω , we henceforth assume that the initial data \mathbf{H}_0 is smooth and is such that $\nabla \cdot (\mu\mathbf{H}_0)|_{\Omega} = 0$ and $\nabla \times \mathbf{H}_0|_{\Omega_v} = 0$. We also assume that either Ω_v is simply connected or that the circulation of \mathbf{H} along any path in the insulating media is zero for all time. The condition $\nabla \times \mathbf{H}|_{\Omega_v} = 0$ together with the above assumption implies that there is a scalar potential ϕ , defined up to an arbitrary constant, such that $\mathbf{H}|_{\Omega_v} = \nabla\phi$. The same holds for \mathbf{H}_0 , i.e., there is ϕ_0 such that $\mathbf{H}_0|_{\Omega_v} = \nabla\phi_0$.

To clarify in which domain we work, we now define

$$\mathbf{H} = \begin{cases} \mathbf{H}^c & \text{in } \Omega_c \\ \nabla\phi & \text{in } \Omega_v, \end{cases} \quad \mu = \begin{cases} \mu^c & \text{in } \Omega_c \\ \mu^v & \text{in } \Omega_v, \end{cases} \tag{2.10}$$

and we denote by \mathbf{n}^c and \mathbf{n}^v the outward normal on $\partial\Omega_c$ and $\partial\Omega_v$, respectively. Similarly, to distinguish between the limits $\lim_{\Omega_{ci} \ni \mathbf{y} \rightarrow \mathbf{x}}$ and $\lim_{\Omega_{cj} \ni \mathbf{y} \rightarrow \mathbf{x}}$ whenever \mathbf{x} is on the interface Σ_μ and $\mathbf{x} \in \overline{\Omega_{ci}} \cap \overline{\Omega_{cj}}$, we set

$$\mathbf{H}_1^c(\mathbf{x}) = \begin{cases} \lim_{\Omega_{ci} \ni \mathbf{y} \rightarrow \mathbf{x}} \mathbf{H}^c(\mathbf{y}) & \text{if } i < j \\ \lim_{\Omega_{cj} \ni \mathbf{y} \rightarrow \mathbf{x}} \mathbf{H}^c(\mathbf{y}) & \text{otherwise,} \end{cases} \quad \mathbf{H}_2^c(\mathbf{x}) = \begin{cases} \lim_{\Omega_{cj} \ni \mathbf{y} \rightarrow \mathbf{x}} \mathbf{H}^c(\mathbf{y}) & \text{if } i < j \\ \lim_{\Omega_{ci} \ni \mathbf{y} \rightarrow \mathbf{x}} \mathbf{H}^c(\mathbf{y}) & \text{otherwise,} \end{cases} \tag{2.11}$$

and we have similar definitions for $\mu_1^c(\mathbf{x})$ and $\mu_2^c(\mathbf{x})$. For any (scalar- or vector-valued) function f that is two-valued at $\mathbf{x} \in \overline{\Omega_{ci}} \cap \overline{\Omega_{cj}}$ we define the average of f at \mathbf{x} as follows:

$$\{f\}(\mathbf{x}) = \frac{1}{2}(f_1(\mathbf{x}) + f_2(\mathbf{x})). \tag{2.12}$$

Furthermore, we denote by $\mathbf{n}^{ci}(\mathbf{x})$ and $\mathbf{n}^{cj}(\mathbf{x})$ the outward normal at \mathbf{x} on $\partial\Omega_{ci}$ and $\partial\Omega_{cj}$, respectively. Assuming that $i < j$, we set $\mathbf{n}_1^c(\mathbf{x}) = \mathbf{n}^{ci}(\mathbf{x})$ and $\mathbf{n}_2^c(\mathbf{x}) = \mathbf{n}^{cj}(\mathbf{x})$.

It is possible to eliminate the electric field from the problem (see e.g. [15] for the details), and once this is done we obtain:

$$\begin{cases} \mu^c\partial_t\mathbf{H}^c = -\nabla \times (R_m^{-1}\sigma^{-1}(\nabla \times \mathbf{H}^c - \mathbf{j}^s) - \tilde{\mathbf{u}} \times \mu^c\mathbf{H}^c), & \text{in every } \Omega_{ci}, i \in \overline{1, N} \\ \mu^v\partial_t\Delta\phi = 0 & \text{in } \Omega_v \\ (R_m^{-1}\sigma^{-1}(\nabla \times \mathbf{H}^c - \mathbf{j}^s) - \tilde{\mathbf{u}} \times \mu^c\mathbf{H}^c) \times \mathbf{n}^c = \mathbf{a} & \text{on } \Gamma_c \\ \mu^v\partial_{\mathbf{n}^v}(\partial_t\phi) = -\mathbf{n}^v \cdot \nabla \times (\mathbf{n}^v \times \mathbf{a}), & \text{on } \Gamma_v \\ \mathbf{H}_1^c \times \mathbf{n}_1^c + \mathbf{H}_2^c \times \mathbf{n}_2^c = 0 & \text{on } \Sigma_\mu \\ \mu_1^c\mathbf{H}_1^c \cdot \mathbf{n}_1^c + \mu_2^c\mathbf{H}_2^c \cdot \mathbf{n}_2^c = 0 & \text{on } \Sigma_\mu \\ \mathbf{H}^c \times \mathbf{n}^c + \nabla\phi \times \mathbf{n}^v = 0 & \text{on } \Sigma \\ \mu^c\mathbf{H}^c \cdot \mathbf{n}^c + \mu^v\nabla\phi \cdot \mathbf{n}^v = 0 & \text{on } \Sigma \\ \mathbf{H}^c|_{t=0} = \mathbf{H}_0, \quad \phi|_{t=0} = \phi_0. \end{cases} \tag{2.13}$$

The first equation in 2.13 is obtained by substituting the electric field in the Faraday equation in the conducting domain by $\mathbf{E}^c := (R_m\sigma)^{-1}(\nabla \times \mathbf{H}^c - \mathbf{j}^s) - \tilde{\mathbf{u}} \times \mu^c\mathbf{H}^c$. The second equation is obtained by taking the divergence of the Faraday equation in the insulating region, $\mu^v\partial_t\nabla\phi = -\nabla \times \mathbf{E}^v$. The third and fourth equations are the boundary condition on the electric field

on $\Gamma_c \cup \Gamma_v$. The fifth, sixth, seventh and eighth equations require that the tangential component of the magnetic field and the normal component of the magnetic induction are continuous across $\Sigma \cup \Sigma_\mu$. Observe that the operator $\mathbf{n}^v \cdot \nabla \times (\cdot)$ involves only tangential derivatives; hence, it is meaningful to have it acting on the field $\mathbf{n}^v \times \mathbf{a}$ which is only defined on Γ . Note also that the two conditions $(\mu^c \mathbf{H}^c \cdot \mathbf{n}^c + \mu^v \nabla \phi \cdot \mathbf{n}^v)|_\Sigma = 0$ and $(\mu_1^c \mathbf{H}^c \cdot \mathbf{n}_1^c + \mu_2^c \mathbf{H}^c \cdot \mathbf{n}_2^c)|_{\Sigma_\mu} = 0$ express the continuity of the normal component of the magnetic induction across Σ and Σ_μ , respectively. These constraints are consequences of the continuity of the tangential components of the electric field across Σ and Σ_μ , respectively.

If the electric field is needed, it is computed in the conducting domain by using Ohm's law, i.e., by setting $\mathbf{E}^c := (R_m \sigma)^{-1} (\nabla \times \mathbf{H}^c - \mathbf{j}^s) - \tilde{\mathbf{u}} \times \mu^c \mathbf{H}^c$. The electric field is computed in the non-conducting medium by solving the Cauchy–Riemann problem: $\nabla \times \mathbf{E}^v = -\mu^v \partial_t \nabla \phi$, $\nabla \cdot \mathbf{E}^v = 0$, $\mathbf{E}^v \times \mathbf{n}^v|_\Sigma = -\mathbf{E}^c \times \mathbf{n}^c|_\Sigma$, $\mathbf{E}^v \times \mathbf{n}^v|_{\Gamma_v} = \mathbf{a}$, and $\int_{\Gamma_v^i} \mathbf{E}^v \cdot \mathbf{n}^v = 0$, $1 \leq i \leq J$. Note that (2.13) does not involve the Γ_v^i 's, $1 \leq i \leq J$, and whether μ is continuous or not does not matter when computing the electric field.

2.5. Weak formulation

A weak formulation of 2.7 with the electric field eliminated (i.e., 2.13) has been derived in [15] assuming that μ is continuous. We handle the discontinuous situation similarly. For this purpose, we introduce the following Hilbert spaces:

$$\mathbf{L} = \{(\mathbf{b}, \varphi) \in \mathbf{L}^2(\Omega_c) \times H^1_{\int=0}(\Omega_v)\}, \tag{2.14}$$

$$\mathbf{X} = \{(\mathbf{b}, \varphi) \in \mathbf{H}_{\text{curl}}(\Omega_c) \times H^1_{\int=0}(\Omega_v); (\mathbf{b} \times \mathbf{n}^c + \nabla \varphi \times \mathbf{n}^v)|_\Sigma = 0\} \tag{2.15}$$

and we equip \mathbf{L} and \mathbf{X} with the norm of $\mathbf{L}^2(\Omega_c) \times H^1(\Omega_v)$ and $\mathbf{H}_{\text{curl}}(\Omega_c) \times H^1(\Omega_v)$, respectively. $H^1_{\int=0}(\Omega_v)$ is the subspace of $H^1(\Omega_v)$ composed of the functions of zero mean value. The space $\mathbf{H}_{\text{curl}}(\Omega_c)$ is composed of the vector-valued functions on Ω_c that are component-wise L^2 -integrable and whose curl is also component-wise L^2 -integrable. The space $\mathbf{H}_{\text{div}}(\Omega)$ is composed of the vector-valued functions on Ω that are component-wise L^2 -integrable and whose divergence is L^2 -integrable. We recall that, for any field \mathbf{b} in $\mathbf{H}_{\text{curl}}(\Omega_c)$, the tangential components of \mathbf{b} are continuous across Σ_μ , i.e., $\mathbf{b}_1 \times \mathbf{n}_1^c + \mathbf{b}_2 \times \mathbf{n}_2^c = 0$.

By proceeding as in [15] and taking inspiration from the so-called Interior Penalty method [2,3], we reformulate the problem as follows: Seek the pair $(\mathbf{H}^c, \phi) \in L^2((0, +\infty); \mathbf{X}) \cap L^\infty((0, +\infty); \mathbf{L})$ (with $\partial_t \mathbf{H}^c$ and $\partial_t \phi$ in appropriate spaces) such that for all pairs $(\mathbf{b}, \varphi) \in \mathbf{X}$ and a.e. $t \in (0, +\infty)$,

$$\left\{ \begin{array}{l} \mathbf{H}^c|_{t=0} = \mathbf{H}_0^c; \quad \nabla \phi|_{t=0} = \nabla \phi_0, \\ \int_{\Omega_c} \left[\mu^c (\partial_t \mathbf{H}^c) \cdot \mathbf{b} + ((R_m \sigma)^{-1} (\nabla \times \mathbf{H}^c - \mathbf{j}^s) - \tilde{\mathbf{u}} \times \mu^c \mathbf{H}^c) \cdot \nabla \times \mathbf{b} \right] + \int_{\Omega_v} \mu^v (\partial_t \nabla \phi) \cdot \nabla \varphi \\ + \int_{\Sigma_\mu} \left\{ (R_m \sigma)^{-1} (\nabla \times \mathbf{H}^c - \mathbf{j}^s) - \tilde{\mathbf{u}} \times \mu^c \mathbf{H}^c \right\} \cdot (\mathbf{b}_1 \times \mathbf{n}_1^c + \mathbf{b}_2 \times \mathbf{n}_2^c) \\ + \int_\Sigma ((R_m \sigma)^{-1} (\nabla \times \mathbf{H}^c - \mathbf{j}^s) - \tilde{\mathbf{u}} \times \mu^c \mathbf{H}^c) \cdot (\mathbf{b} \times \mathbf{n}^c + \nabla \varphi \times \mathbf{n}^v) \\ = \int_{\Gamma_c} (\mathbf{a} \times \mathbf{n}) \cdot (\mathbf{b} \times \mathbf{n}) + \int_{\Gamma_v} (\mathbf{a} \times \mathbf{n}) \cdot (\nabla \varphi \times \mathbf{n}). \end{array} \right. \tag{2.16}$$

The interface integrals over Σ and Σ_μ are zero since $\mathbf{b} \times \mathbf{n}^c + \nabla \varphi \times \mathbf{n}^v = 0$ and $\mathbf{b}_1 \times \mathbf{n}_1^c + \mathbf{b}_2 \times \mathbf{n}_2^c = 0$, but we nevertheless retain these two integrals since they will not vanish when we construct the non-conforming finite element approximation, see Section 3. In the same spirit, observe that the tangential components of the average of $\{((R_m \sigma)^{-1} (\nabla \times \mathbf{H}^c - \mathbf{j}^s) - \tilde{\mathbf{u}} \times \mu^c \mathbf{H}^c)\} \times \mathbf{n}_1^c$ are equal to the average of the tangential components of the electric field. Since the tangential components of electric field are continuous, the two terms composing the average across Σ_μ are actually equal. We nevertheless retain the average notation since this is the formulation that we shall use when we construct the non-conforming finite element approximation, see Section 3.

The main novelty with respect to [15,16] is the presence in 2.16 of the boundary integral over Σ_μ . It is this term that will allow us to account for jumps on the magnetic permeability. The boundary integral over Σ_μ appears when one tests the Faraday equation in 2.13 with a test function \mathbf{b} that is piecewise smooth on $\Omega_{c1}, \dots, \Omega_{cN}$ but with discontinuous tangential components across Σ_μ , and when one integrates by parts over each Ω_{ci} , $i \in \overline{1, N}$.

Showing that the problem 2.16 is well-posed under suitable assumption on the velocity field $\tilde{\mathbf{u}}$ is a standard exercise in functional analysis; it is essentially a consequence of Lions' theorem (see e.g. [p.218][6], [pp.253–258][22]). We refer e.g. [1,5], [Thm 2.1][15] for more details on the well-posedness issue.

At this point it may not seem clear to the reader that the weak formulation (2.16) naturally enforces the interface condition $\mu_1^c \mathbf{H}_1^c \cdot \mathbf{n}_1^c + \mu_2^c \mathbf{H}_2^c \cdot \mathbf{n}_2^c = 0$ across Σ_μ . To see that this is indeed true, let us set $\mathbf{E}^c := (R_m \sigma)^{-1} (\nabla \times \mathbf{H}^c - \mathbf{j}^s) - \tilde{\mathbf{u}} \times \mu^c \mathbf{H}^c$ on Ω_c . By using test functions compactly supported on Ω_c , one infers from 2.16 that \mathbf{H}^c and \mathbf{E}^c are related by Faraday's law: $\mu^c \partial_t \mathbf{H}^c = -\nabla \times \mathbf{E}^c$ (integrate by parts over Ω_c and apply a distribution argument). Similarly, by using test functions whose support is compact on Ω_c and has a non-empty intersection with Σ_μ , one infers from 2.16 that the tangential components of \mathbf{E}^c are continuous across Σ_μ , i.e., $\mathbf{E}_1^c \times \mathbf{n}_1^c + \mathbf{E}_2^c \times \mathbf{n}_2^c = 0$ (integrate by parts over Ω_{c1} and over Ω_{c2}). This immediately implies that $(\nabla \times \mathbf{E}_1^c) \cdot \mathbf{n}_1^c + (\nabla \times \mathbf{E}_2^c) \cdot \mathbf{n}_2^c = 0$ across Σ_μ , which, owing to Faraday's law, implies $\partial_t (\mu_1 \mathbf{H}_1^c \cdot \mathbf{n}_1^c + \mu_2 \mathbf{H}_2^c \cdot \mathbf{n}_2^c) = 0$ across Σ_μ . One then concludes that $\mu_1 \mathbf{H}_1^c \cdot \mathbf{n}_1^c + \mu_2 \mathbf{H}_2^c \cdot \mathbf{n}_2^c = 0$ across Σ_μ , since this relation holds at time $t = 0$, (recall that \mathbf{H}_0 is smooth and $\nabla \cdot (\mu^c \mathbf{H}_0) = 0$ in Ω_c).

3. Approximation

The purpose of this section is to explain how (2.16) is discretized in space and time. We proceed as in [15,16], taking into account that μ^c is discontinuous, but the divergence-free condition on the magnetic induction is treated differently so as to handle quite general geometries.

3.1. The geometry

The algorithm that we propose takes advantage of the cylindrical symmetry of the domain Ω and the interfaces Σ and Σ_μ . The symmetry axis is denoted Oz and the cylindrical coordinates are denoted (r, θ, z) : r is the distance to the Oz axis; θ , ($0 \leq \theta \leq 2\pi$), is the angular coordinate; and z is the position along the Oz axis. We denote by $\Omega_v^{2D}, \Omega_c^{2D}$ and Ω_{ci}^{2D} ($i = 1, \dots, N$), the meridional sections of Ω_v, Ω_c and Ω_{ci} , respectively. We assume that Ω_v, Ω_c and Ω_{ci} have piecewise quadratic boundaries. These sections are meshed using quadratic triangular meshes.

We denote by $\{\mathcal{F}_h^v\}_{h>0}, \{\mathcal{F}_h^c\}_{h>0}$ and $\{\mathcal{F}_h^{ci}\}_{h>0}$ the corresponding regular families of non-overlapping quadratic triangular meshes. We assume for the sake of simplicity that, for every given mesh index h , \mathcal{F}_h^{ci} is a subset of \mathcal{F}_h^c . We denote by Σ_h^{2D} and $\Sigma_{\mu h}^{2D}$ the collection of triangle faces that compose the meridional section of Σ and Σ_μ , respectively. The collection of cylindrical surfaces generated by rotation around the symmetry axis by the faces in Σ_h^{2D} and $\Sigma_{\mu h}^{2D}$ are denoted by Σ_h and $\Sigma_{\mu h}$, respectively. For every cylindrical surface F in $\Sigma_h \cup \Sigma_{\mu h}$, we denote by h_F the diameter of the triangle face that generates F .

For every element K in the mesh $\mathcal{F}_h^v \cup \mathcal{F}_h^c$ we denote by $T_K: \hat{K} \rightarrow K$ the quadratic transformation that maps the reference triangle $\hat{K} := \{(\hat{r}, \hat{z}) \in \mathbb{R}^2, 0 \leq \hat{r}, 0 \leq \hat{z}, \hat{r} + \hat{z} \leq 1\}$ to K , and we denote by h_K the diameter of K . Finally, we denote by K^{3D} the volume generated by rotation around the symmetry axis by an element K .

3.2. Space discretization for the Maxwell equations

The electromagnetic part of the problem is approximated by using the technique introduced in [15]. The main feature of the space approximation is that the method is non-conforming, i.e., the continuity constraint $(\mathbf{b} \times \mathbf{n}^c + \nabla\varphi \times \mathbf{n}^v)|_\Sigma = 0$ and $(\mathbf{b}_1 \times \mathbf{n}_1^c + \mathbf{b}_2 \times \mathbf{n}_2^c)|_{\Sigma_\mu} = 0$ in \mathbf{X} (see (2.15)) are relaxed and enforced by means of an interior penalty method.

Let ℓ_H and ℓ_ϕ be two integers in $\{1, 2\}$ with $\ell_\phi \geq \ell_H$. We first define the meridional finite element spaces

$$\mathbf{X}_h^{H,2D} := \left\{ \mathbf{b}_h \in \mathbf{L}^2(\Omega_c); \mathbf{b}_h|_{\Omega_{ci}} \in \mathcal{C}^0(\overline{\Omega_{ci}}), \forall i = 1, \dots, N, \mathbf{b}_h(T_K)|_K \in \mathbb{P}_{\ell_H}, \forall K \in \mathcal{F}_h^c \right\}, \tag{3.1}$$

$$X_h^{\phi,2D} := \left\{ \varphi_h \in \mathcal{C}^0(\overline{\Omega_v}); \varphi_h(T_K)|_K \in \mathbb{P}_{\ell_\phi}, \forall K \in \mathcal{F}_h^v \right\}, \tag{3.2}$$

where \mathbb{P}_k denotes the set of bivariate polynomials of total degree at most k , and $\mathbb{P}_k := \mathbb{P}_k \times \mathbb{P}_k \times \mathbb{P}_k$. Then, using the complex notation $i^2 = -1$, the magnetic field and the scalar potential are approximated in the following spaces:

$$\mathbf{X}_h^H := \left\{ \mathbf{b} = \sum_{m=-M}^M \mathbf{b}_h^m(r, z) e^{im\theta}; \mathbf{b}_h^m \in \mathbf{X}_h^{H,2D}, \overline{\mathbf{b}_h^m} = \mathbf{b}_h^{-m}, k \in \overline{0, M} \right\}, \tag{3.3}$$

$$X_h^\phi := \left\{ \varphi = \sum_{m=-M}^M \varphi_h^m(r, z) e^{im\theta}; \varphi_h^m \in X_h^{\phi,2D}, \overline{\varphi_h^m} = \varphi_h^{-m}, m \in \overline{0, M} \right\}, \tag{3.4}$$

where $M + 1$ is the maximum number of complex Fourier modes.

3.3. Time discretization

We use the same time discretization as in [16]. We just recall the main steps without going through the details. The time derivatives are approximated using the second-order Backward Difference Formula (BDF2). All the terms that are likely to mix the modes are made explicit (e.g. cross products). Let Δt be the time step and set $t^n := n\Delta t$, $n \geq 0$. A first version of the algorithm is written as follows: after appropriate initialization at t^0 and t^1 , define the following fields for all $n \geq 1$

$$\mathbf{H}^* = 2\mathbf{H}^{c,n} - \mathbf{H}^{c,n-1} \tag{3.5}$$

$$\begin{cases} D\mathbf{H}^{c,n+1} := \frac{1}{2}(3\mathbf{H}^{c,n+1} - 4\mathbf{H}^{c,n} + \mathbf{H}^{c,n-1}), \\ D\phi^{n+1} := \frac{1}{2}(3\phi^{n+1} - 4\phi^n + \phi^{n-1}). \end{cases} \tag{3.6}$$

The solution to the Maxwell part of the problem is computed in one step by solving for $\mathbf{H}^{c,n+1}$ in \mathbf{X}_h^H and ϕ^{n+1} in X_h^ϕ so that the following holds for all \mathbf{b} in \mathbf{X}_h^H and all φ in X_h^ϕ

$$\int_{\Omega_c} \mu^c \frac{D\mathbf{H}^{c,n+1}}{\Delta t} \cdot \mathbf{b} + \int_{\Omega_v} \mu^v \frac{\nabla D\phi^{n+1}}{\Delta t} \cdot \nabla\varphi + \mathcal{L}((\mathbf{H}^{c,n+1}, \phi^{n+1}), (\mathbf{b}, \varphi)) = \mathcal{R}_n(\mathbf{b}, \varphi), \tag{3.7}$$

where we have defined the linear form \mathcal{R}_n

$$\begin{aligned} \mathcal{R}_n(\mathbf{b}, \varphi) := & \int_{\Gamma_v} (\mathbf{a} \times \mathbf{n}^v) \cdot (\nabla \varphi \times \mathbf{n}^v) + \int_{\Gamma_c} (\mathbf{a} \times \mathbf{n}^c) \cdot (\mathbf{b} \times \mathbf{n}^c) + \int_{\Omega_c} ((R_m \sigma)^{-1} \mathbf{j}^s + \tilde{\mathbf{u}} \times \mu^c \mathbf{H}^*) \cdot \nabla \times \mathbf{b} \\ & + \int_{\Sigma_\mu} \{ (R_m \sigma)^{-1} \mathbf{j}^s + \tilde{\mathbf{u}} \times \mu^c \mathbf{H}^* \} \cdot \llbracket \mathbf{b} \times \mathbf{n} \rrbracket + \int_{\Sigma} ((R_m \sigma)^{-1} \mathbf{j}^s + \tilde{\mathbf{u}} \times \mu^c \mathbf{H}^*) \cdot (\mathbf{b} \times \mathbf{n}^c + \nabla \varphi \times \mathbf{n}^v) \end{aligned}$$

and $\llbracket \mathbf{b} \times \mathbf{n} \rrbracket$ stands for $\mathbf{b}_1 \times \mathbf{n}_1^c + \mathbf{b}_2 \times \mathbf{n}_2^c$. The bilinear form \mathcal{L} in (3.7) is defined by

$$\begin{aligned} \mathcal{L}((\mathbf{H}^{c,n+1}, \phi^{n+1}), (\mathbf{b}, \varphi)) := & \int_{\Omega_c} (R_m \sigma)^{-1} \nabla \times \mathbf{H}^{c,n+1} \cdot \nabla \times \mathbf{b} + \int_{\Sigma_\mu} \{ (R_m \sigma)^{-1} \nabla \times \mathbf{H}^{c,n+1} \} \cdot \llbracket \mathbf{b} \times \mathbf{n} \rrbracket \\ & + g((\mathbf{H}^{c,n+1}, \phi^{n+1}), (\mathbf{b}, \varphi)) + \int_{\Sigma} (R_m \sigma)^{-1} \nabla \times \mathbf{H}^{c,n+1} \cdot (\mathbf{b} \times \mathbf{n}^c + \nabla \varphi \times \mathbf{n}^v) \end{aligned}$$

where g is defined by

$$\begin{aligned} g((\mathbf{H}^{c,n+1}, \phi^{n+1}), (\mathbf{b}, \varphi)) := & \beta_2 \sum_{F \in \Sigma_{\mu h}} h_F^{-1} \int_F \llbracket \mathbf{H}^{c,n+1} \times \mathbf{n}^c \rrbracket \cdot \llbracket \mathbf{b} \times \mathbf{n}^c \rrbracket \\ & + \beta_1 \sum_{F \in \Sigma_h} h_F^{-1} \int_F (\mathbf{H}^{c,n+1} \times \mathbf{n}^c + \nabla \phi^{n+1} \times \mathbf{n}^v) \cdot (\mathbf{b} \times \mathbf{n}^c + \nabla \varphi \times \mathbf{n}^v), \end{aligned} \tag{3.8}$$

The purpose of the bilinear form g is to penalize the quantities $\mathbf{H}^{c,n+1} \times \mathbf{n}^c + \nabla \phi^{n+1} \times \mathbf{n}^v$ and $\llbracket \mathbf{H}^{c,n+1} \times \mathbf{n}^c \rrbracket$ across Σ and Σ_μ , respectively, so that they converge to zero when the mesh-size goes to zero. The coefficients β_1 and β_2 are user-dependent. We usually take

$$\beta_1 = \gamma_1 / (R_m \min_{\mathbf{x} \in \Omega_c} (\sigma(\mathbf{x}))), \quad \beta_2 = \gamma_2 / (R_m \min_{\mathbf{x} \in \Omega_c} (\sigma(\mathbf{x}))),$$

with $\gamma_1 = \gamma_2 = 1$. This scaling can be justified by arguments from the Interior Penalty theory [2,15,16].

3.4. Addition of a magnetic pressure

At this point, the only novelty with respect to [16] is that the approximate magnetic field is discontinuous across the interface $\Sigma_{\mu h}$. This method has been proven to be convergent on finite time intervals, but it may fail to converge in the steady state regime. Indeed, in the time-dependent case, taking the divergence of Faraday's equation, we observe that provided the initial magnetic induction is divergence-free, the following holds for all times

$$\nabla \cdot (\mu \mathbf{H}) = 0.$$

Unfortunately, in the steady state case, this condition is a constraint that the above technique may fail to respect. We describe in this section the modifications we have made in order to enforce the divergence-free condition in both conducting and insulating part, even in time-independent situations.

3.4.1. Motivation for a magnetic pressure

In [16], the solenoidality constraint is enforced by means of a penalty term added to the bilinear form \mathcal{L} , namely

$$\beta_0 \int_{\Omega_c} \nabla \cdot (\mu^c \mathbf{H}^{c,n+1}) \cdot \nabla \cdot (\mu^c \mathbf{b}),$$

where $\beta_0 = 0$ or 1 depending on the regularity of the domain. Taking $\beta_0 = 1$ requires that the approximate solution converges to the exact solution in the $\mathbf{H}_{\text{curl}} \cap \mathbf{H}_{\text{div}}$ norm. We point out the fact that we want to use \mathbf{H}^1 -conforming Lagrange finite elements. It is known since the ground-breaking work of Costabel (cf. [7]) that, for non-smooth and non-convex domains (e.g. a L-shape domain), \mathbf{H}^1 is a genuine closed subspace of $\mathbf{H}_{\text{curl}} \cap \mathbf{H}_{\text{div}}$. This means that one can find elements in $\mathbf{H}_{\text{curl}} \cap \mathbf{H}_{\text{div}}$ that cannot be approximated by elements of \mathbf{H}^1 . We thus need to find another way to deal with the divergence-free constraint in non-smooth domains.

3.4.2. In the conducting region

Taking inspiration from [4], we propose a non standard technique, which consists of replacing the induction equation in the conducting part by

$$\partial_t (\mu^c \mathbf{H}^c) = -\nabla \times \mathbf{E}^c - \mu^c \nabla p^c, \quad (-\Delta_0)^\alpha p^c = -\nabla \cdot (\mu^c \mathbf{H}^c), \quad p^c|_{\partial \Omega_c} = 0, \tag{3.9}$$

where α is a yet-to-be-chosen real parameter, Δ_0 is the Laplace operator on Ω_c with zero Dirichlet boundary condition, and p^c is a new scalar unknown which we call magnetic pressure. A simple calculation shows that if the initial magnetic induction is solenoidal, then $p^c \equiv 0$ so that (3.9) indeed enforces the condition $\nabla \cdot (\mu^c \mathbf{H}^c) = 0$. Taking $\alpha = 0$ in the above formulation amounts to penalize $\nabla \cdot (\mu^c \mathbf{H}^c)$ in $L^2(\Omega_c)$, as in the previous subsection. For $\alpha \in (\frac{1}{2}, 1]$, this new formulation can be shown to be convergent, even if the domain is non-smooth and non-convex. We refer to [4] for the mathematical analysis of this

method. Although $\alpha = 1$ is a legitimate value when solving boundary value problems, it is shown in [4] that α should be taken away from 1 when solving eigenvalue problems in non-smooth domains to avoid spurious eigenvalues. In practice, we use $\alpha \in [0.6, 0.8]$ and we do not observe any significative dependence of the method with respect to α when the interfaces are non-smooth. When the interfaces are smooth the method works properly for any value $\alpha \in [0, 1]$ both for boundary value and eigenvalue problems.

3.4.3. In the vacuum

We proceed slightly differently in Ω_v . The induction equation is replaced by the following

$$\partial_t(\mu^v \nabla \phi) = -\nabla \times \mathbf{E}^v - \mu^v \nabla p^v, \quad \Delta p^v = \Delta \phi, \quad \nabla p^v \cdot \mathbf{n}^v|_{\partial\Omega_v} = 0, \quad (3.10)$$

where p^v is a new scalar unknown, and μ^v is the magnetic permeability in the vacuum which we assume to be constant. Once again, a simple calculation shows that if the initial magnetic induction is solenoidal, then $p^v \equiv 0$, so that (3.10) indeed enforces $\Delta \phi = 0$. Moreover, upon observing that

$$\int_{\Omega_v} \nabla p^v \cdot \nabla \phi = \int_{\Omega_v} \nabla \phi \cdot \nabla \phi - \int_{\partial\Omega_v} (\mathbf{n} \cdot \nabla \phi) \phi, \quad \forall \phi \in H^1(\Omega_v)$$

The weak formulation of (3.10) can be re-written as follows:

$$\int_{\Omega_v} \mu^v (\partial_t \nabla \phi) \cdot \nabla \phi = - \int_{\Omega_v} \nabla \times \mathbf{E}^v \cdot \nabla \phi - \int_{\Omega_v} \mu^v \nabla \phi \cdot \nabla \phi + \int_{\partial\Omega_v} \mu^v (\mathbf{n} \cdot \nabla \phi) \phi, \quad \forall \phi \in H^1(\Omega_v)$$

so that p^v is eliminated from the formulation.

3.4.4. Final algorithm

Finally, we have three unknown fields (one vector-field \mathbf{H}^c , two scalar fields ϕ, p^c) instead of two (\mathbf{H}^c, ϕ).

We introduce a new finite element space to approximate the new scalar unknown p^c :

$$X_h^{p,2D} := \left\{ p_h \in L^2(\Omega_c) / p_h \in C^0(\overline{\Omega_c}), p_h(T_K) \in \mathbb{P}_{\ell_p}, \forall K \in \mathcal{F}_h^c, p_h = 0 \text{ on } \partial\Omega_c \right\},$$

$$X_h^p := \left\{ p = \sum_{m=-M}^M p_h^m(r, z) e^{im\theta} / \forall m = 1 \dots, M, p^m \in X_h^{p,2D} \text{ and } p_h^m = \overline{p_h^{-m}} \right\}.$$

Here ℓ_p is an integer in $\{1, 2\}$.

The final form of the algorithm is the following: after proper initialization, we solve for $\mathbf{H}^{c,n+1} \in \mathbf{X}_h^H, \phi^{n+1} \in X_h^\phi$ and $p^{c,n+1} \in X_h^p$ so that the following holds for all $\mathbf{b} \in \mathbf{X}_h^H, \psi \in X_h^\phi, q \in X_h^p$

$$\int_{\Omega_c} \mu^c \frac{D\mathbf{H}^{c,n+1}}{\Delta t} \cdot \mathbf{b} + \int_{\Omega_v} \mu^v \frac{\nabla D\phi^{n+1}}{\Delta t} \cdot \nabla \phi + \mathcal{L}((\mathbf{H}^{c,n+1}, \phi^{n+1}), (\mathbf{b}, \phi)) + \mathcal{P}(\phi^{n+1}, \phi) + \mathcal{D}((\mathbf{H}^{c,n+1}, p^{c,n+1}), (\mathbf{b}, q)) = \mathcal{R}_n(\mathbf{b}, \phi) \quad (3.11)$$

where \mathcal{P} denotes the stabilizing bilinear form defined by

$$\mathcal{P}(\phi, \psi) = \int_{\Omega_v} \mu^v \nabla \phi \cdot \nabla \psi - \int_{\partial\Omega_v} \mu^v \psi \mathbf{n} \cdot \nabla \phi$$

and \mathcal{D} is defined by

$$\mathcal{D}((\mathbf{H}, p), (\mathbf{b}, q)) := \beta_0 \left(\int_{\Omega_c} \mu^c \nabla p \cdot \mathbf{b} - \int_{\Omega_c} \mu^c \mathbf{H} \cdot \nabla q + \sum_{K \in \mathcal{F}_h^c} \int_{K^{3D}} h_K^{2(1-\alpha)} \nabla p \cdot \nabla q + s(\mathbf{H}^{c,n+1}, \mathbf{b}) \right),$$

where the last bilinear form s is defined by

$$s(\mathbf{H}, \mathbf{b}) := \sum_{K \in \mathcal{F}_h^c} \int_{K^{3D}} h_K^{2\alpha} \nabla \cdot (\mu^c \mathbf{H}) \nabla \cdot (\mu^c \mathbf{b}).$$

\mathcal{P} accounts for the addition of p^v and \mathcal{D} is a discrete approximation for the weak formulation of (3.9). Finally, s is a stabilization term that makes the discrete formulation well-posed irrespective of the polynomial degree of the approximation for p^c . The coefficient β_0 is scaled as follows:

$$\beta_0 = \gamma_0 / (R_m \min_{\mathbf{x} \in \Omega_c} (\sigma(\mathbf{x}))),$$

with $\gamma_0 = 1$. This scaling can be justified by arguments from the Interior Penalty theory [2,15,16].

4. Convergence tests

The new formulation 3.11 presents two major novelties with respect to that introduced in [16]: it now accounts for non-smooth geometries and discontinuous magnetic permeability fields. The purpose of this section is to illustrate numerically these new features on benchmark problems.

4.1. The L-shape domain

We first illustrate the positive effect of the magnetic pressure in the case of steady-state regime in a non-smooth and non-convex domain. The setting is the following: we consider the conducting L-shape domain (two dimensional case)

$$\Omega = \Omega_c = (-1, +1)^2 \setminus ([0, +1] \times [-1, 0]). \tag{4.1}$$

with no insulating region, $\Omega_p = \emptyset$, (cf. Fig. 2). We take $\mu = 1$, $\tilde{\mathbf{u}} = 0$, and $\sigma = 1$.

4.1.1. Boundary value problem

Consider the following boundary value problem in the above defined L-shape domain: find \mathbf{H} such that

$$\nabla \times \nabla \times \mathbf{H} = 0, \quad \nabla \cdot \mathbf{H} = 0, \quad \mathbf{H} \times \mathbf{n}|_{\Gamma} = \mathbf{G} \times \mathbf{n}, \tag{4.2}$$

where the Cartesian components of the boundary data \mathbf{G} are given by

$$\mathbf{G}(r, \theta) = \frac{2}{3} r^{-\frac{1}{3}} \begin{pmatrix} -\sin\left(\frac{\theta}{3}\right) \\ \cos\left(\frac{\theta}{3}\right) \end{pmatrix} \tag{4.3}$$

and (r, θ) are the polar coordinates centered at the re-entrant corner of the domain. The solution to the above problem is $\mathbf{H} = \nabla \psi$, where $\psi(r, \theta) = r^{\frac{2}{3}} \sin\left(\frac{2}{3}\theta\right)$.

Five quasi-uniform (non-nested) Delaunay meshes are considered of mesh-sizes $h = 1/10, 1/20, 1/40, 1/80, 1/160$, respectively. The meshes are composed of triangles. Two types of approximation are tested; we use \mathbb{P}_1 elements in the first case and \mathbb{P}_2 elements in the second case. The magnetic field and the magnetic pressure are approximated using equal order polynomials in each case.

Denoting by \mathbf{H}_h the approximate magnetic field, we report in Table 1 the relative errors $\|\mathbf{H}_h - \mathbf{H}\|_{\mathbf{L}^2} / \|\mathbf{H}\|_{\mathbf{L}^2}$ for $\alpha = 0.75$ and $\alpha = 1$. Table 1 also shows the computed order of convergence (COC). Convergence is observed for the \mathbb{P}_1 and \mathbb{P}_2 approximations. The best possible convergence rate is $\frac{2}{3}$ and this rate is achieved numerically when using \mathbb{P}_2 elements.

4.1.2. Eigenvalue problem

We now study Ohmic decay in the conducting L-shape domain. Assuming that the magnetic field has the following behavior $\mathbf{H}(\mathbf{x}, t) = \mathbf{H}(\mathbf{x}) e^{-\lambda t}$, where $\lambda > 0$, we are lead to consider the following eigenvalue problem: find (λ, \mathbf{H}) such that

$$\nabla \times \nabla \times \mathbf{H} = \lambda \mathbf{H}, \quad \nabla \cdot \mathbf{H} = 0, \quad \mathbf{H} \times \mathbf{n}|_{\Gamma} = 0, \tag{4.4}$$

Approximations of the first five eigenvalues with 10^{-11} tolerance are provided in [9]: $\lambda_1 \approx 1.47562182408$, $\lambda_2 \approx 3.53403136678$, $\lambda_3 = \lambda_4 = \pi^2 \approx 9.86960440109$, and $\lambda_5 \approx 11.3894793979$. We solve 4.4 using ARPACK [20] with a relative tolerance of 10^{-8} .

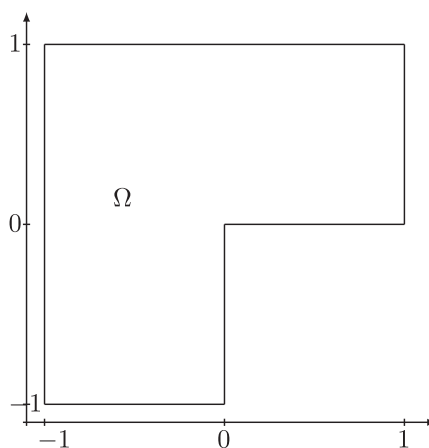


Fig. 2. Two-dimensional L-shape domain with constant μ^c .

Table 1

$L^2(\Omega)$ relative errors and computed order of convergence for the boundary value problem (4.2) and (4.3) using \mathbb{P}_1 elements (2nd and 3rd columns) and \mathbb{P}_2 elements (4th and 5th columns) with $\alpha = 0.75$ and $\alpha = 1$; h is the typical diameter of the Delaunay meshes.

h	\mathbb{P}_1				\mathbb{P}_2			
	$\alpha = 0.75$		$\alpha = 1$		$\alpha = 0.75$		$\alpha = 1$	
	Rel. Error	COC						
0.1	$2.390 \cdot 10^{-1}$	N/A	$2.303 \cdot 10^{-1}$	N/A	$1.290 \cdot 10^{-1}$	N/A	$1.110 \cdot 10^{-1}$	N/A
0.05	$1.843 \cdot 10^{-1}$	0.38	$1.826 \cdot 10^{-1}$	0.34	$8.178 \cdot 10^{-2}$	0.66	$7.016 \cdot 10^{-2}$	0.66
0.025	$1.405 \cdot 10^{-1}$	0.39	$1.367 \cdot 10^{-1}$	0.42	$5.978 \cdot 10^{-2}$	0.45	$5.017 \cdot 10^{-2}$	0.48
0.0125	$1.031 \cdot 10^{-1}$	0.45	$1.010 \cdot 10^{-1}$	0.44	$3.759 \cdot 10^{-2}$	0.67	$3.191 \cdot 10^{-2}$	0.65
0.00625	$7.544 \cdot 10^{-2}$	0.45	$7.656 \cdot 10^{-2}$	0.4	$2.232 \cdot 10^{-2}$	0.75	$1.938 \cdot 10^{-2}$	0.72

Table 2 shows the first eigenvalue computed with $\alpha = 0.9$ on five quasi-uniform (non-nested) Delaunay meshes of mesh-sizes $1/10, 1/20, 1/40, 1/80, 1/160$, respectively. As explained in [4], taking α close to 1 improves the convergence rate on the first eigenvalue. The method is clearly convergent although the eigenvector has a strong unbounded singularity.

Table 3 shows the first five eigenvalues computed with $\alpha = 0.7$ on five quasi-uniform (non-nested) Delaunay meshes of mesh-sizes $1/10, 1/20, 1/40, 1/80, 1/160$, respectively. Here again we observe convergence and there is no spurious eigenvalue. As expected the worst rate of convergence is observed for the first eigenvalue which corresponds to the most singular eigenvector. The second eigenvector is in $H^1(\Omega)$, the third and fourth eigenvectors are analytic, the fifth one has a strong unbounded singularity. The theory developed in [4] shows that the accuracy of the method improves when $\alpha \rightarrow 1$, but the absence of spurious eigenvalues is assured only for $\alpha < 1$. This phenomenon can be observed on the first eigenvalue by comparing Tables 2 and 3. The COC stalls for the eigenvalues λ_3 and λ_4 using \mathbb{P}_2 since the accuracy of the computed eigenvalues is limited by the tolerance in ARPACK (10^{-8}).

4.2. Induction in a composite sphere

We now turn our attention to three-dimensional induction problems with discontinuous permeability fields.

4.2.1. Description of the problem

The domain is $\Omega := \mathbb{R}^3$ and the conductor is composed of two concentric spheres centered at 0 . The radius of the inner sphere, say Ω_1 , is R_1 and its magnetic permeability is μ_1 . The radius of the outer conducting sphere, say Ω_2 , is R_2 and its magnetic permeability is μ_2 . This composite sphere is surrounded by vacuum of magnetic permeability μ_0 . The magnetic field at infinity is the vertical uniform field $\mathbf{H}_0 := H_0 \mathbf{e}_z$. The magnetic field solves

$$\nabla \times \mathbf{H} = 0, \quad \nabla \cdot (\mu \mathbf{H}) = 0, \quad \lim_{\|\mathbf{x}\| \rightarrow +\infty} \mathbf{H}_0(\mathbf{x}) = H_0 \mathbf{e}_z. \tag{4.5}$$

This problem has an analytical steady state solution which is derived in [10] and which we briefly recall for the sake of completeness.

There is a scalar potential ψ so that $\mathbf{H} = \nabla \psi$ in \mathbb{R}^3 , and ψ solves $\nabla \cdot (\mu \nabla \psi) = 0$ in \mathbb{R}^3 with $\nabla \psi \rightarrow H_0 \mathbf{e}_z$ at infinity. Using the spherical coordinates $(\varrho, \vartheta, \theta)$, where ϱ is the distance to the origin, $\vartheta \in [0, \pi]$ is the colatitude and $\theta \in [0, 2\pi)$ is the azimuth, the potential is given by

$$\psi(\varrho, \vartheta, \theta) = \begin{cases} -A\varrho \cos \vartheta, & \text{for } \varrho \leq R_1 \\ -\left(B\varrho + C \frac{R_1^3}{\varrho^2}\right) \cos \vartheta & \text{for } R_1 \leq \varrho \leq R_2 \\ -\left(D \frac{R_1^3}{\varrho^2} - H_0 \varrho\right) \cos \vartheta & \text{for } R_2 \leq \varrho, \end{cases} \tag{4.6}$$

where A, B, C and D are constants. The constants can be computed by enforcing ψ and $\mu \partial_\varrho \psi$ to be continuous across Σ_μ and Σ , (the continuity of ψ guarantees that the tangential components of the magnetic field \mathbf{H} are continuous and the continuity

Table 2

Relative errors and COC for λ_1 using \mathbb{P}_1 elements and \mathbb{P}_2 elements with $\alpha = 0.9$. The symbol “–” indicates that the pair (Linear Solver + ARPACK) did not converge with the assigned tolerances.

h	\mathbb{P}_1			\mathbb{P}_2		
	λ_1	Rel. Error	COC	λ_1	Rel. Error	COC
0.1	1.555	$5.256 \cdot 10^{-2}$	N/A	1.508	$2.192 \cdot 10^{-2}$	N/A
0.05	1.541	$4.353 \cdot 10^{-2}$	0.27	1.493	$1.167 \cdot 10^{-2}$	0.9
0.025	1.522	$3.094 \cdot 10^{-2}$	0.49	1.487	$7.371 \cdot 10^{-3}$	0.66
0.0125	1.507	$2.126 \cdot 10^{-2}$	0.54	1.481	$3.726 \cdot 10^{-3}$	0.98
0.00625	1.497	$1.465 \cdot 10^{-2}$	0.54	–	–	N/A

Table 3

First five eigenvalues using \mathbb{P}_1 elements and \mathbb{P}_2 elements with $\alpha = 0.7$. The symbol “-” indicates that the pair (Linear Solver + ARPACK) did not converge with the assigned tolerances.

h	\mathbb{P}_1			\mathbb{P}_2		
	λ_i	Rel. Error	COC	λ_i	Rel. Error	COC
0.1	1.930	$2.668 \cdot 10^{-1}$	N/A	1.707	$1.452 \cdot 10^{-1}$	N/A
0.05	1.845	$2.224 \cdot 10^{-1}$	0.26	1.623	$9.522 \cdot 10^{-2}$	0.61
0.025	1.765	$1.788 \cdot 10^{-1}$	0.32	1.586	$7.240 \cdot 10^{-2}$	0.4
0.0125	1.696	$1.389 \cdot 10^{-1}$	0.36	1.545	$4.614 \cdot 10^{-2}$	0.65
0.00625	1.644	$1.080 \cdot 10^{-1}$	0.36	-	-	N/A
0.1	3.573	$1.101 \cdot 10^{-2}$	N/A	3.537	$8.266 \cdot 10^{-4}$	N/A
0.05	3.551	$4.716 \cdot 10^{-3}$	1.22	3.535	$2.380 \cdot 10^{-4}$	1.8
0.025	3.540	$1.578 \cdot 10^{-3}$	1.58	3.534	$6.640 \cdot 10^{-5}$	1.8
0.0125	3.536	$6.245 \cdot 10^{-4}$	1.33	3.534	$1.726 \cdot 10^{-5}$	1.9
0.00625	3.535	$2.768 \cdot 10^{-4}$	1.17	-	-	N/A
0.1	5.450	$5.770 \cdot 10^{-1}$	N/A	7.828	$2.307 \cdot 10^{-1}$	N/A
0.05	7.852	$2.277 \cdot 10^{-1}$	1.34	9.870	$3.799 \cdot 10^{-7}$	19.21
0.025	9.873	$3.075 \cdot 10^{-4}$	2.89	9.870	$3.856 \cdot 10^{-8}$	3.3
0.0125	9.870	$7.714 \cdot 10^{-5}$	2.0	9.870	$3.444 \cdot 10^{-8}$	0.16
0.00625	9.870	$1.934 \cdot 10^{-5}$	2.0	-	-	N/A
0.1	5.455	$5.761 \cdot 10^{-1}$	N/A	7.841	$2.291 \cdot 10^{-1}$	N/A
0.05	7.858	$2.270 \cdot 10^{-1}$	1.34	9.870	$4.712 \cdot 10^{-7}$	18.9
0.025	9.873	$3.100 \cdot 10^{-4}$	9.52	9.870	$3.856 \cdot 10^{-8}$	3.61
0.0125	9.870	$7.768 \cdot 10^{-5}$	2.0	9.870	$1.990 \cdot 10^{-8}$	0.95
0.00625	9.870	$1.935 \cdot 10^{-5}$	2.0	-	-	N/A
0.1	5.506	$6.964 \cdot 10^{-1}$	N/A	7.903	$3.614 \cdot 10^{-1}$	N/A
0.05	7.877	$3.646 \cdot 10^{-1}$	0.93	11.39	$2.374 \cdot 10^{-5}$	13.89
0.025	11.39	$4.326 \cdot 10^{-4}$	9.72	11.39	$7.786 \cdot 10^{-6}$	1.61
0.0125	11.39	$1.457 \cdot 10^{-4}$	1.57	11.39	$2.168 \cdot 10^{-6}$	1.85
0.00625	11.39	$5.303 \cdot 10^{-5}$	1.46	-	-	N/A

of $\mu \partial_\varrho \psi$ guarantees that the normal component of the magnetic induction $\mu \mathbf{H}$ is continuous). To simplify the expressions of A, B, C and D we assume that $\mu_1 = \mu_0$ and we abuse the notation by setting $\mu := \mu_2/\mu_0$. Then,

$$A = - \frac{9\mu H_0}{(2\mu + 1)(\mu + 2) - 2(\mu - 1)^2 \left(\frac{R_1}{R_2}\right)^3}$$

$$D = \frac{(2\mu + 1)(\mu - 1) \left[\left(\frac{R_2}{R_1}\right)^3 - 1\right] H_0}{(2\mu + 1)(\mu + 2) - 2(\mu - 1)^2 \left(\frac{R_1}{R_2}\right)^3}$$

$$B = \frac{1}{3} \left(2 + \frac{1}{\mu}\right) A, \quad C = \frac{1}{3} \left(1 - \frac{1}{\mu}\right) A.$$

The magnetic field in Ω_1 is $\mathbf{H}|_{\Omega_1} = -A\mathbf{e}_z$. Whether the spheres are composed of conducting material or not does not matter since the conductivity coefficient does not appear in any formula. As a result, the inner sphere can be viewed from two different perspectives: we can either consider Ω_1 to be part of the conducting medium (with $\mu_1 = \mu_0$), in which case $\Omega_c = \Omega_1 \cup \Omega_2$, or we can consider Ω_1 to be part of the non-conducting medium, in which case $\Omega_c = \Omega_2$. Both cases are described by the same steady solution but the numerical approximations computed by our method are computed differently.

Note that $A \rightarrow 0, B \rightarrow 0, C \rightarrow 0, D \rightarrow (R_2/R_1)^3 H_0$, and $\mu B \rightarrow 3 H_0/(1 - (R_1/R_2)^3), \mu C \rightarrow 6H_0/(1 - (R_1/R_2)^3)$ when $\mu \rightarrow \infty$; as a result, the magnetic field tends to zero in $\Omega_1 \cup \Omega_2$ but the magnetic induction converges to a non-zero limit in Ω_2 when $\mu \rightarrow \infty$. The magnetic field penetrates more or less in the spheres depending on the value of μ , and it is completely expelled from the spheres in the limit $\mu \rightarrow \infty$.

4.2.2. Case 1: Inner sphere is a conductor

We assume that $\Omega_c = \Omega_1 \cup \Omega_2$, i.e., the conducting medium is composed of the inner and the outer spheres. We take $\mathcal{L} := R_2$ as reference length scale and we set $R_1 = \frac{1}{2}R_2$. We set $\mathcal{H} := H_0$ to non-dimensionalize the magnetic field since there is no velocity to construct a reference magnetic field.

The infinite vacuum region is truncated at $\varrho = 10R_2$. We enforce the time-independent Dirichlet condition $\phi = H_0 z := H_0 \varrho \cos\vartheta$ at the outer boundary of the vacuum region, Γ_v . The steady solution is computed in one time step using $\Delta t = 10^9$. (Recall that the steady-state problem is now well-posed thanks to our introducing the magnetic pressure.)

The above problem is solved using various uniformly refined meshes and various values of μ . The stabilizing exponent α is equal to 0.75. The magnetic pressure is approximated using \mathbb{P}_1 elements, the magnetic field is approximated using \mathbb{P}_2

elements, and the scalar potential is approximated using \mathbb{P}_2 elements. For each computation we measure the relative error on \mathbf{H}^c , $\nabla \times \mathbf{H}^c$, $\nabla \cdot (\mu^c \mathbf{H}^c)$ in the $L^2(\Omega_c)$ -norm, and the error on ϕ in the $H^1(\Omega_v)$ -norm. The results are reported in Table 4. The method converges well in the range $\mu \in [2, 200]$.

Fig. 3 shows the computed solution for $\mu = 200$. We observe that the radial component H_r^c (panel (a)) is continuous at ($\varrho = R_1$ and $\vartheta = 0, \vartheta = \pi$) and that the vertical component H_z^c (panel (b)) is continuous at ($\varrho = R_1, \vartheta = \pi/2$). This shows that the IP method enforces well the continuity of the tangential component of the magnetic field. The panel (c) shows the magnetic field lines of \mathbf{H}^c ($0 \leq \varrho \leq R_2$) and those of $\nabla \phi$ ($R_2 \leq \varrho$). The magnetic lines in the vacuum region arrive nearly perpendicularly at the ferromagnetic interface. This phenomenon is a feature of $\mu \rightarrow \infty$.

4.2.3. Case 2: Hollow sphere

We use the same geometric setting as in case 1, but we now assume that the inner sphere is an insulator, i.e., $\Omega_c = \Omega_2$. The non-conducting medium, Ω_v , is composed of the inner sphere Ω_1 plus the spherical annulus $\varrho \in (R_2, 10R_2)$. The exact solution to this problem is the same as in case 1.

We repeat the same convergence tests as in case 1. The results are reported in Table 5. We observe that the method converges well in the range $\mu \in [2, 200]$ and that the convergence rates are almost identical to those shown in Table 4.

4.3. Induction in rotating devices

We test in this section the proposed method on rotating conductors embedded in a uniform external magnetic field. We make two numerical tests: the first one assesses the robustness of the method with respect to geometrical singularities and the second one assesses the robustness of the method with respect to high permeability contrasts. These tests have been preformed with $\alpha = 0.7$.

4.3.1. Induction in a finite rotating solid cylinder

Let Ω_c be a conducting cylinder of non-dimensional radius $R = 1$ and height $L_z^c = 1.6$. This cylinder is embedded in vacuum in \mathbb{R}^3 and rotates about the z-axis with angular speed $\varpi = 1$. (The reference velocity \mathcal{U} is equal to the product of the radius of the cylinder and the angular velocity.) The non-dimensional conductivity is $\sigma = 1$ and the magnetic Reynolds number is $R_m = 100$. The non-dimensional magnetic permeability in the entire electromagnetic domain is constant and equal to one, i.e., $\mu^c = \mu^v = 1$. The imposed magnetic field at infinity is $H_0 \mathbf{e}_x$. This is a benchmark test case thoroughly investigated in [31].

The time-dependent problem is solved with initial data $\mathbf{H}_0 = H_0 \mathbf{e}_x$ on a Delaunay mesh which is quasi-uniform in the conducting region and of mesh-size $h = 1/100$. We use \mathbb{P}_2 elements for both the magnetic field and the magnetic potential. The magnetic pressure is approximated using \mathbb{P}_1 elements. The time step is $\Delta t = 5 \cdot 10^{-2}$. The truncated numerical domain is $\Omega = \{r \in (0, 1.6), \theta \in [0, 2\pi], z \in (-4, 4)\}$ and the non-conducting domain is $\Omega_v = \Omega \setminus \Omega_c$. The imposed boundary condition on Γ_v is $\phi|_{\Gamma_v} = H_0 r \cos \theta$. The only active Fourier mode is $m = 1$.

The time evolution of the magnetic energy is shown in Fig. 4a. The graph shows oscillations that correspond to reconnections of the magnetic lines. Fig. 4b shows the radial profile of H_z at $z = 0.8$ in the meridian plane $\theta = 0$ at steady state. Note that the point $r = 1, \theta = 0, z = 0.8$ is located on the upper sharp edge of the cylinder. The profile is compared with that obtained in [31]. The agreement is excellent considering that the gradient of the solution is discontinuous at the edges of the cylinder.

Fig. 5a,b show the contour lines of the $m = 1$ azimuthal Fourier mode of H_θ at $t = 100$. Observe that H_θ is symmetric with respect to the equatorial plane. Plotting the contour lines of H_θ emphasizes the skin effect. The lines shown in Fig. 5a, b are very close to those reported in Fig. 5 from [31] even at the corners. Fig. 5c shows the streamlines of the Fourier mode $m = 1$ of the electric current in the cylinder. The current is mainly contained in a thin layer (of the order of the skin depth). It varies

Table 4

Case 1, $\mathbb{P}_2/\mathbb{P}_2$; one iteration ($\Delta t = 10^0$); $\alpha = 0.75$.

μ	h	\mathbf{H}, L^2	COC	$\nabla \times \mathbf{H}, L^2$	COC	$\nabla \cdot (\mu^c \mathbf{H}^c), L^2$	COC	ϕ, H^1	COC
2	0.16	$1.688 \cdot 10^{-3}$	-	$7.328 \cdot 10^{-3}$	-	$2.665 \cdot 10^{-2}$	-	$9.536 \cdot 10^{-5}$	-
	0.08	$2.691 \cdot 10^{-4}$	2.65	$2.094 \cdot 10^{-3}$	1.81	$1.068 \cdot 10^{-2}$	1.32	$2.018 \cdot 10^{-5}$	2.24
	0.04	$3.898 \cdot 10^{-5}$	2.79	$4.889 \cdot 10^{-4}$	2.10	$3.831 \cdot 10^{-3}$	1.48	$3.431 \cdot 10^{-6}$	2.56
	0.02	$7.088 \cdot 10^{-6}$	2.46	$1.239 \cdot 10^{-4}$	1.98	$1.480 \cdot 10^{-3}$	1.37	$5.945 \cdot 10^{-7}$	2.53
	0.01	$1.363 \cdot 10^{-6}$	2.38	$3.114 \cdot 10^{-5}$	1.99	$5.980 \cdot 10^{-4}$	1.31	$1.032 \cdot 10^{-7}$	2.53
20	0.16	$8.044 \cdot 10^{-3}$	-	$3.729 \cdot 10^{-2}$	-	$1.314 \cdot 10^{-2}$	-	$3.218 \cdot 10^{-4}$	-
	0.08	$1.004 \cdot 10^{-3}$	3.00	$6.180 \cdot 10^{-3}$	2.59	$6.699 \cdot 10^{-3}$	0.97	$7.065 \cdot 10^{-5}$	2.19
	0.04	$1.089 \cdot 10^{-4}$	3.21	$4.273 \cdot 10^{-4}$	3.85	$1.845 \cdot 10^{-3}$	1.86	$1.253 \cdot 10^{-5}$	2.50
	0.02	$2.048 \cdot 10^{-5}$	2.41	$4.570 \cdot 10^{-5}$	3.22	$4.856 \cdot 10^{-4}$	1.93	$2.220 \cdot 10^{-6}$	2.50
	0.01	$3.832 \cdot 10^{-6}$	2.42	$1.069 \cdot 10^{-5}$	2.10	$1.310 \cdot 10^{-4}$	1.89	$3.885 \cdot 10^{-7}$	2.51
200	0.16	$1.067 \cdot 10^{-1}$	-	$3.728 \cdot 10^{-1}$	-	$3.876 \cdot 10^{-3}$	-	$3.984 \cdot 10^{-4}$	-
	0.08	$2.439 \cdot 10^{-2}$	2.13	$9.239 \cdot 10^{-2}$	2.01	$2.620 \cdot 10^{-3}$	0.57	$8.331 \cdot 10^{-5}$	2.26
	0.04	$4.321 \cdot 10^{-3}$	2.50	$1.571 \cdot 10^{-2}$	2.56	$1.076 \cdot 10^{-3}$	1.28	$1.444 \cdot 10^{-5}$	2.53
	0.02	$6.547 \cdot 10^{-4}$	2.72	$2.233 \cdot 10^{-3}$	2.81	$4.114 \cdot 10^{-4}$	1.39	$2.577 \cdot 10^{-6}$	2.49
	0.01	$9.008 \cdot 10^{-5}$	2.86	$2.956 \cdot 10^{-4}$	2.92	$1.223 \cdot 10^{-4}$	1.75	$4.536 \cdot 10^{-7}$	2.51

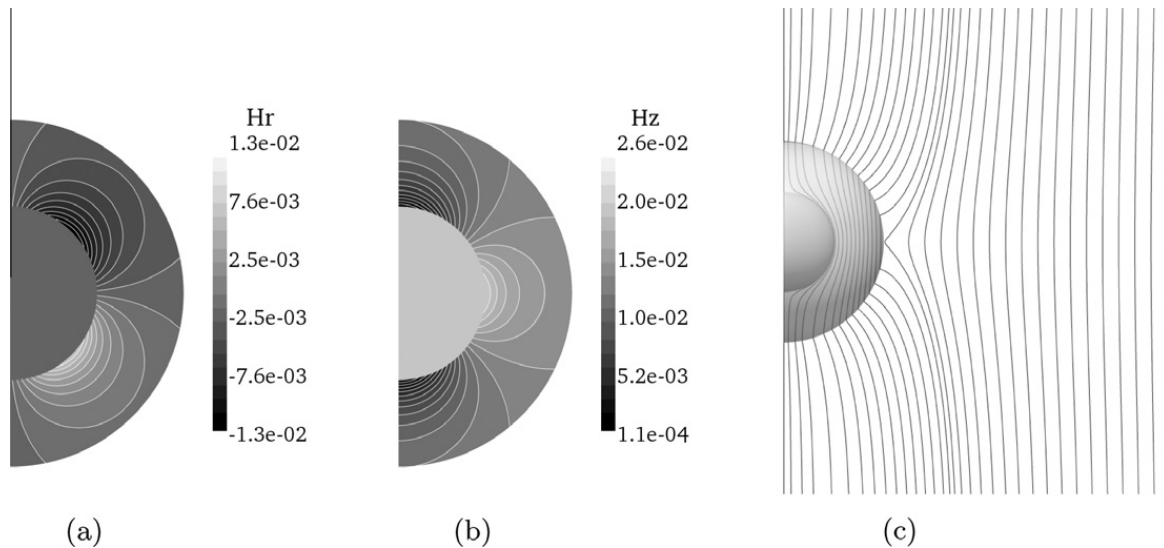


Fig. 3. Steady solution for a composite sphere embedded in a vertical uniform magnetic field: (a–b) H_r and H_z for conducting inner and outer spheres with relative permeability $\mu = 200$; (c) magnetic field lines.

Table 5

Case 2, $\mathbb{P}2/\mathbb{P}2$; one iteration ($\Delta t = 10^9$); $\alpha = 0.75$.

μ	h	\mathbf{H}, L^2	COC	$\nabla \times \mathbf{H}, L^2$	COC	$\nabla \cdot (\mu^c \mathbf{H}^c), L^2$	COC	ϕ, H^1	COC
2	0.16	$1.590 \cdot 10^{-3}$	–	$7.314 \cdot 10^{-3}$	–	$2.424 \cdot 10^{-2}$	–	$1.362 \cdot 10^{-4}$	–
	0.08	$2.913 \cdot 10^{-4}$	2.45	$2.002 \cdot 10^{-3}$	1.87	$9.423 \cdot 10^{-3}$	1.36	$2.679 \cdot 10^{-5}$	2.35
	0.04	$2.898 \cdot 10^{-5}$	3.33	$4.525 \cdot 10^{-4}$	2.15	$3.285 \cdot 10^{-3}$	1.52	$3.924 \cdot 10^{-6}$	2.77
	0.02	$4.910 \cdot 10^{-6}$	2.56	$1.088 \cdot 10^{-4}$	2.06	$1.189 \cdot 10^{-3}$	1.47	$6.694 \cdot 10^{-7}$	2.55
	0.01	$1.109 \cdot 10^{-6}$	2.15	$2.665 \cdot 10^{-5}$	2.03	$4.637 \cdot 10^{-4}$	1.36	$1.162 \cdot 10^{-7}$	2.53
20	0.16	$9.418 \cdot 10^{-3}$	–	$3.924 \cdot 10^{-2}$	–	$1.282 \cdot 10^{-2}$	–	$3.423 \cdot 10^{-4}$	–
	0.08	$1.494 \cdot 10^{-3}$	2.66	$6.749 \cdot 10^{-3}$	2.54	$6.627 \cdot 10^{-3}$	0.95	$7.261 \cdot 10^{-5}$	2.24
	0.04	$1.952 \cdot 10^{-4}$	2.94	$5.859 \cdot 10^{-4}$	3.53	$1.832 \cdot 10^{-3}$	1.85	$1.245 \cdot 10^{-5}$	2.54
	0.02	$2.409 \cdot 10^{-5}$	3.02	$7.075 \cdot 10^{-5}$	3.05	$4.819 \cdot 10^{-4}$	1.93	$2.203 \cdot 10^{-6}$	2.50
	0.01	$2.889 \cdot 10^{-6}$	3.06	$1.255 \cdot 10^{-5}$	2.49	$1.291 \cdot 10^{-4}$	1.90	$3.862 \cdot 10^{-7}$	2.51
200	0.16	$1.098 \cdot 10^{-1}$	–	$3.934 \cdot 10^{-1}$	–	$3.861 \cdot 10^{-3}$	–	$4.013 \cdot 10^{-4}$	–
	0.08	$2.474 \cdot 10^{-2}$	2.15	$9.847 \cdot 10^{-2}$	2.00	$2.596 \cdot 10^{-3}$	0.57	$8.380 \cdot 10^{-5}$	2.26
	0.04	$4.415 \cdot 10^{-3}$	2.49	$1.740 \cdot 10^{-2}$	2.50	$1.067 \cdot 10^{-3}$	1.28	$1.472 \cdot 10^{-5}$	2.51
	0.02	$7.451 \cdot 10^{-4}$	2.57	$2.658 \cdot 10^{-3}$	2.71	$4.091 \cdot 10^{-4}$	1.38	$2.642 \cdot 10^{-6}$	2.48
	0.01	$1.211 \cdot 10^{-4}$	2.62	$3.999 \cdot 10^{-4}$	2.73	$1.217 \cdot 10^{-4}$	1.75	$4.668 \cdot 10^{-7}$	2.50

smoothly in the azimuthal direction and bends sharply at the corners. This behavior is a direct consequence of the presence of the cylindrical interface with vacuum. The current creates the z-component of the magnetic field and is responsible for the strong extremum of H_z at the sharp edges of the cylinder ($r = 1, \theta \in [0, 2\pi], z = \pm 0.8$).

4.3.2. Induction in counter-rotating disks made of soft iron

In order to measure the impact of soft iron disks on induction fields, we now consider two counter-rotating disks embedded in a cylindrical conductor which is itself embedded in vacuum. This test case is a qualitative illustration of the Cadarache VKS2 fluid dynamo studied in more details in Section 5.

The conducting domain is a cylinder of non-dimensional radius $R = 1$ and of rectangular cross section of non-dimensional height $L = 2.55$: $\Omega_c = \{(r, \theta, z); r \in [0, 1], z \in (-1.275, 1.275), \theta \in [0, 2\pi)\}$. Two counter-rotating disks, $\Omega_c^{\text{top}}, \Omega_c^{\text{bot}}$, are embedded in Ω_c . The upper rotating conducting disk is a cylinder whose cross section is defined as follows:

$$\begin{cases} 0.775 \leq z \leq 0.975 & \text{if } r \leq 0.65, \\ (r - 0.65)^2 + (z - 0.875)^2 \leq (0.1)^2 & \text{if } r \geq 0.65. \end{cases}$$

The lower rotating conducting disk is the image by reflection about the equatorial plane $z = 0$ of the upper disk. There is no analytical solution to this problem, but asymptotic solutions are given in [17] assuming that the disks are of rectangular cross section. The upper and lower disks rotate with non-dimensional angular speed $\varpi_{\text{top}} = -1$ and $\varpi_{\text{bot}} = 1$, respectively. The non-dimensional magnetic permeability and conductivity of the non-rotating solid container, $\Omega_c \setminus (\Omega_c^{\text{top}} \cup \Omega_c^{\text{bot}})$, are $\mu_0 = 1$ and $\sigma_0 = 1$, respectively. The non-dimensional magnetic permeability and conductivity of the two counter-rotating

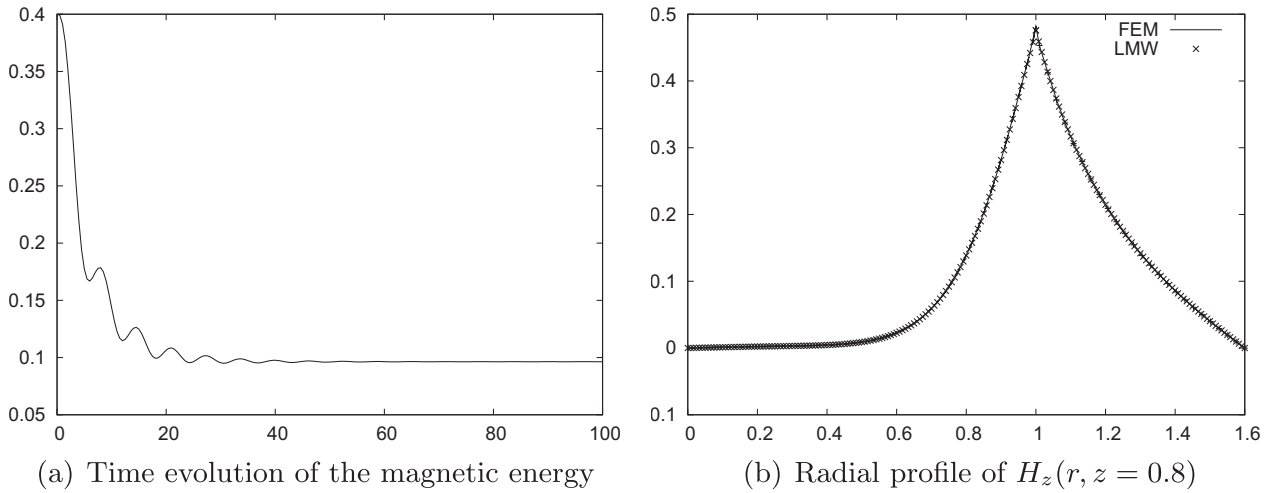


Fig. 4. Induction in a finite rotating solid cylinder at $R_m = 100$. 'LMW' is the result from [31], 'FEM' is our result with \mathbb{P}_2 finite elements for \mathbf{H} and \mathbb{P}_2 finite elements for ϕ with $h = 1/100$.

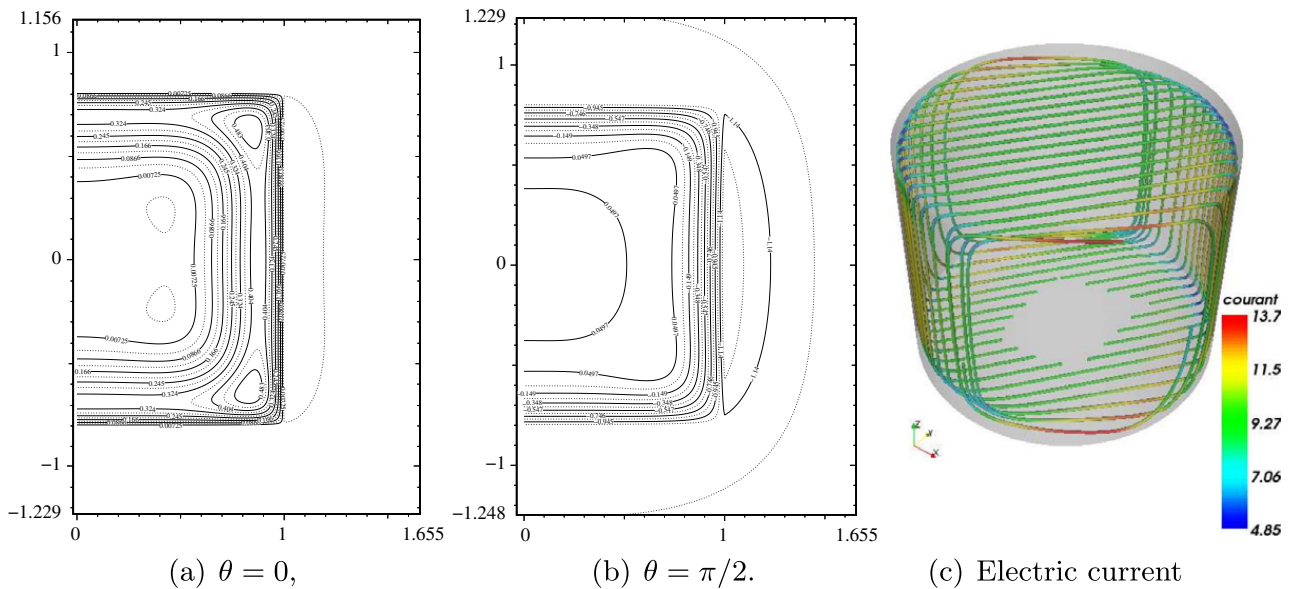


Fig. 5. Rotating cylinder at $R_m = 100$ at steady state. Contours of H_θ of the $m = 1$ mode in azimuthal planes and streamlines of the electric current of the $m = 1$ mode colored by the norm of the current.

disks, $\Omega_c^{\text{top}} \cup \Omega_c^{\text{bot}}$, are μ_d and σ_d , respectively. The non-dimensional magnetic permeability of the vacuum is $\mu_0 = 1$. The imposed velocity field in Ω_c is

$$\tilde{\mathbf{u}}^{n+1}(\mathbf{x}) = \begin{cases} 0 & \text{in } \Omega_c \setminus (\Omega_c^{\text{top}} \cup \Omega_c^{\text{bot}}) \\ \varpi_{\text{top}} \mathbf{e}_z \times \mathbf{x} & \text{in } \Omega_c^{\text{top}} \\ \varpi_{\text{bot}} \mathbf{e}_z \times \mathbf{x} & \text{in } \Omega_c^{\text{bot}} \end{cases}$$

The device is placed in a transverse uniform magnetic field $\mathbf{H}_0 := H_0 \mathbf{e}_x = H_0(\cos\theta \mathbf{e}_r - \sin\theta \mathbf{e}_\theta)$ and we look for the steady state solution in two cases: (a) $\mu_d = 200\mu_0$, $\sigma_d = 1$; (b) $\mu_d = 1$, $\sigma_d = 200\sigma_0$. In both cases the effective magnetic Reynolds number is the same for the disks $R_m^{\text{disks}} = \mu_d \sigma_d \varpi_{\text{bot}} R^2 = 200\mu_0 \sigma_0$.

For computational purposes the vacuum region is truncated and restricted to the sphere of non-dimensional radius $R_v = 10$. The time-independent Dirichlet condition $\phi = H_0 r \cos\theta$ is enforced at the outer boundary of the vacuum region, Γ_v . The steady solution is computed by advancing 3.11 in time until convergence to steady state is reached. We use the $\mathbb{P}_2/\mathbb{P}_2$ finite element pair for \mathbf{H} and ϕ and \mathbb{P}_1 elements for the magnetic pressure.

Some three-dimensional representations of the computed solutions are shown in Fig. 6. Panels (a) and (d) show some magnetic field streamlines near the top disk seen from the side of the cylinder. Panels (b) and (e) show the same magnetic field streamlines seen from the top of the cylinder. Panels (c) and (f) show the contour of the magnetic energy corresponding

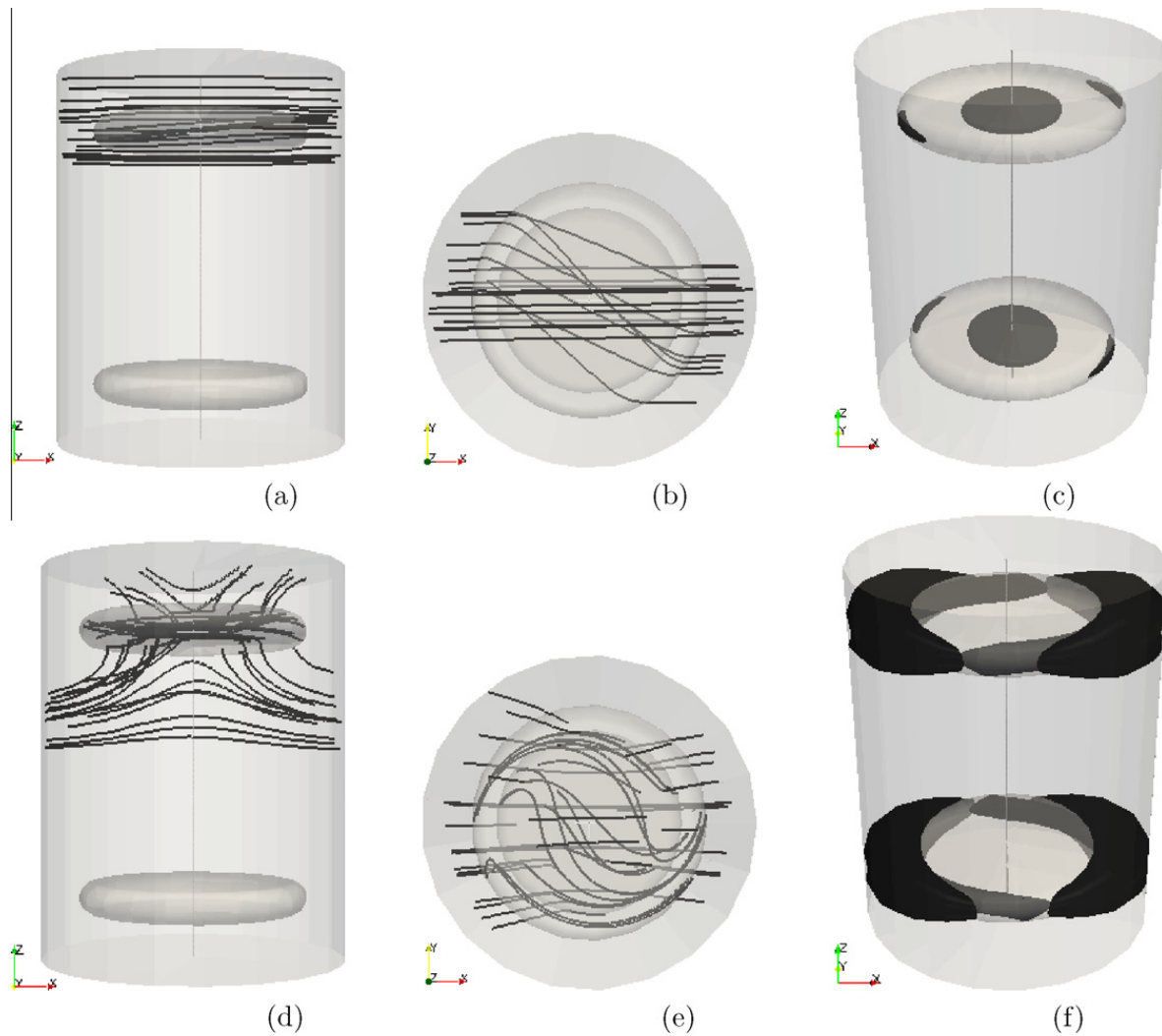


Fig. 6. Steady solutions for two counter-rotating disks in a cylindrical vessel: (a,b,c) $\mu_d = \mu_0$ and $\sigma_d = 200 \sigma_0$; (c,d,e) $\mu_d = 200\mu_0$ and $\sigma_d = \sigma_0$; magnetic line near the top disk seen from the side (a,d) and from the top (b,e); (c,f) contours corresponding to 10% of the maximum magnetic energy.

to 10% of the maximum energy. The top panels (a,b,c) correspond to the solution with $\mu_d = \mu_0$ and $\sigma_d = 200\sigma_0$ and the bottom panels (d,e,f) correspond to the solution with $\mu_d = 200\mu_0$ and $\sigma_d = \sigma_0$. The two steady solutions are very different although the two configurations have the same effective magnetic Reynolds number. When the disks are non-ferromagnetic, the magnetic field lines are distorted horizontally due to the eddy current in each disk. When the disks are ferromagnetic, the field lines are distorted inside the disks but also outside as they connect nearly perpendicularly to the disks.

5. Kinematic dynamo

The kinematic code based on the new formulation 3.11 has been further validated on kinematic dynamo problems by making comparisons with a finite-volume/boundary-element method code [13] using analytical axisymmetric flows. We now illustrate the efficiency of the new method by applying it to VKS2-like kinematic dynamo problems. These tests have been performed with $\alpha = 0.7$.

5.1. The VKS2 experiment

The interest of the scientific community for dynamo action in liquid metals has been renewed since 2000 in the wake of successful experiments [11,30,26]. We show in this section that the numerical method proposed in this paper is suitable, to some extent, to model the Cadarache von Kármán Sodium 2 (VKS2) experiment [26] which has been done in liquid sodium.

The experimental set-up is schematically represented on Fig. 7 together with the simplified geometry that we use in the numerical simulations. The 'bulk flow', composed of liquid sodium, is contained in a cylinder of radius $r = 206$ mm, height 524 mm and thickness 5 mm. This cylinder is made of copper and is henceforth referred to as the envelope. The liquid sodium is stirred by two counter-rotating impellers located at the top and bottom of the container. Each impeller is

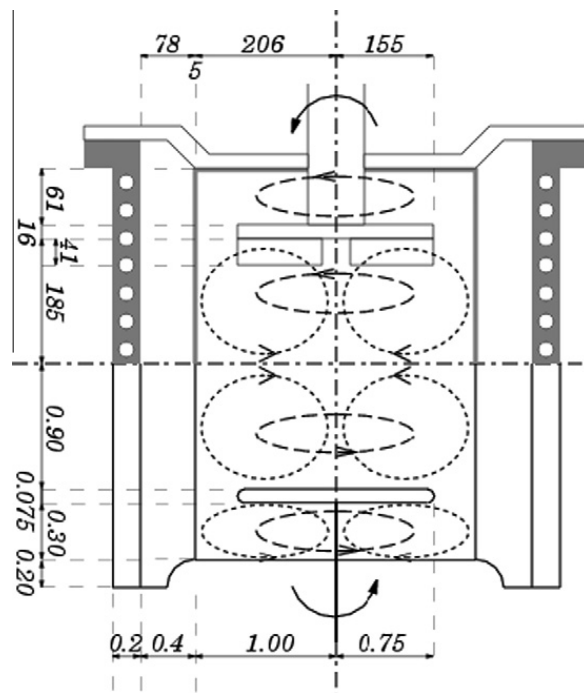


Fig. 7. VKS design and mean-flow structure. Top: dimensions (in millimeters) and technical details of the set-up. Are represented the copper vessel with the embedded cooling system, the thin copper envelope of radius $r = 206$ mm, height 524 mm and thickness 5 mm separating the flow and the stagnant liquid sodium, the impellers (disks with attached blades), and the shafts (courtesy of the VKS team). Bottom: simplified geometry in non-dimensional units for numerical simulations; the thickness of the copper envelope is zero.

composed of a supporting disk and eight curved blades. The impellers act on the liquid sodium as efficient centrifugal pumps: the fluid is pumped in and expelled out radially, thus forming an helicoidal flow. The top and bottom flows recirculate alongside the envelope wall and meet at the mid-plane. This creates a strong azimuthal shear-layer between the two toroidal recirculation flows. A layer of stationary liquid sodium is trapped between the envelope and the cooling system. This stationary fluid zone is called 'side layer'. Due to experimental and technical constraints, two additional layers of liquid sodium exist between the impellers and the top and bottom lids of the copper container and are referred to as 'lid flows'.

Dynamo action was first observed in the VKS2 set-up once the two counter-rotating impellers, which were initially made of stainless steel, were replaced by soft iron ones and the injected power was high enough [26]. Once dynamo action occurs, the measured time-averaged magnetic field is that of a steady axisymmetric axial dipole with a strong azimuthal component in the equatorial plane [25]. This contradicts the kinematic dynamo computations based on axisymmetric time-averaged von Kármán flows reported in [23,28,29,18,21]. In these simulations the generated magnetic field is non-axisymmetric as a consequence of Cowling's theorem [8] (the Fourier mode $m = 1$ is always found to be the most unstable mode). Until now, there is no satisfying explanation that could throw light on the generation of the mainly axisymmetric magnetic field which is observed in the VKS2 experiment. Cowling's theorem [8] implies that there exists a mechanism in the VKS2 experiment that breaks the flow axisymmetry, and this mechanism has yet to be clearly identified. One possible scenario to explain this behavior is that small scale helical turbulence may have induction effects via the so called α -effect. A source for the α -effect could be the helical flow induced by the shear between outwardly expelled fluid trapped between the impeller blades and the slower moving fluid in the bulk of the container [19,27,12].

Another possible scenario proposed in [14] is based on non-axisymmetric velocity fluctuations created by nonlinearities on the induction equation.

Notwithstanding the above scenarios, recent experimental observations (F. Daviaud, private communication, 2010) have shown that the role of moving ferromagnetic material is crucial. With the same available power, the dynamo effect has been obtained only when at least one of the rotating impellers is made of soft iron. In particular, the following material substitutions have led to subcritical behavior: (1) replacing the copper envelope by a soft iron one while using steel impellers, (2) using steel impellers enclosed in a copper envelope and filling the space occupied by the 'lid flow' with copper plates, (3) using one non-rotating impeller (disk + blades) made of soft iron, the other rotating impeller being made of steel, and removing the envelope, (4) placing non-rotating soft iron disk behind the steel impellers and removing the envelope, (5) using two rotating composite impellers (either composed of soft iron disks with steel blades or steel disks with soft iron blades) and removing the envelope. The main conclusion of all these experiments is that at least one of the impellers (disk + blades) must be made of soft iron and must rotate for the dynamo effect to be observed.

Obviously the experiment is quite complex. The purpose of the present study is not to explain the generation of the observed axisymmetric magnetic field in the VKS2 experiment but rather to investigate the role played by the magnetic

permeability of the impellers on the dynamo threshold for the $m = 1$ Fourier mode. That this mode has not been observed may be related to the limited range of magnetic Reynolds numbers available in the VKS device ($R_m \leq 50$).

5.2. Simplified model

Before going through the analysis of a VKS2-like device we investigate the effect of the 'side layer' and compare the so-called vanishing tangential field (VTF) boundary condition with the vacuum boundary condition. The VTF boundary condition, $\mathbf{H} \times \mathbf{n}|_r = 0$, models walls of infinite permeability.

We consider two simplified geometries of the VKS device. The first one (vessel Nb1) is a cylinder of rectangular cross section $(r, z) \in [0, 1.6R_0] \times [-\frac{1}{2}H_0, \frac{1}{2}H_0]$ with $H_0 = 1.8R_0$. The moving fluid is contained in the cylinder of cross section $(r, z) \in [0, R_0] \times [-\frac{1}{2}H_0, \frac{1}{2}H_0]$ and the 'side layer' is the torus of cross section $(r, z) \in [R_0, 1.4R_0] \times [-\frac{1}{2}H_0, \frac{1}{2}H_0]$. The outer part of the vessel of cross section $(r, z) \in [1.4R_0, 1.6R_0] \times [-\frac{1}{2}H_0, \frac{1}{2}H_0]$ is made of copper, cf. Fig. 8a. The second simplified vessel (vessel Nb2) is a cylinder of rectangular cross section $(r, z) \in [0, R_0] \times [-\frac{1}{2}H_0, \frac{1}{2}H_0]$ with $H_0 = 1.8R_0$ filled with moving fluid cf. Fig. 8b. Note that the impellers are not accounted for in these two simplified models. The conductivity of the fluid is σ_0 and that of copper is $\sigma = 4.5\sigma_0$. The magnetic permeability is assumed to be uniformly constant, μ_0 .

Three different kinematic dynamo scenarii with prescribed velocity field $\tilde{\mathbf{u}}$ are considered:

- Case 1 The conducting region is vessel Nb1. The device is embedded in a truncated sphere of vacuum of radius $10R_0$. The usual vacuum/conductor transmission conditions are enforced on the interface Σ which separate the conducting material from the vacuum region (see 2.13).
- Case 2 The conducting region is again modeled by the vessel Nb1, but in order to replicate the VKS2 experiment, we now model the presence of soft iron impellers at the top and bottom of the moving fluid region by enforcing the infinite permeability boundary condition $\mathbf{H} \times \mathbf{n} = 0$ at $\{z = \pm \frac{1}{2}H_0, 0 \leq r \leq R_0\}$. The device is again embedded in a truncated sphere of vacuum of radius $10R_0$. The usual vacuum/conductor transmission conditions are enforced on the remaining part of the interface Σ where the VTF condition is not applied (see 2.13).
- Case 3 The conducting region is modeled by the vessel Nb2. The infinite permeability boundary condition $\mathbf{H} \times \mathbf{n} = 0$ is enforced on the entire boundary of the vessel. This boundary condition is expected to model an envelope made of soft iron in the VKS2 experiment. There is no insulating region.

The velocity field $\tilde{\mathbf{u}}$ that has been chosen for these tests is the axisymmetric time-averaged flow field measured in a water experiment which is documented in [28]. The flow is interpolated on the finite element grid and normalized by the maximum of the euclidian norm of the velocity, U_{\max} . Henceforth we use $\mathcal{L} = R_0$ as reference length scale and $\mathcal{U} = U_{\max}$ as reference velocity scale. The magnetic Reynolds number is

$$R_m = \mu_0 \sigma_0 U_{\max} R_0. \tag{5.1}$$

From Cowling's theorem [8], only magnetic fields with Fourier modes $m \geq 1$ can be generated by a prescribed axisymmetric velocity field. Furthermore, the azimuthal modes are uncoupled since $\nabla \times (\tilde{\mathbf{u}} \times \mathbf{H}^c)$ cannot transfer energy between the

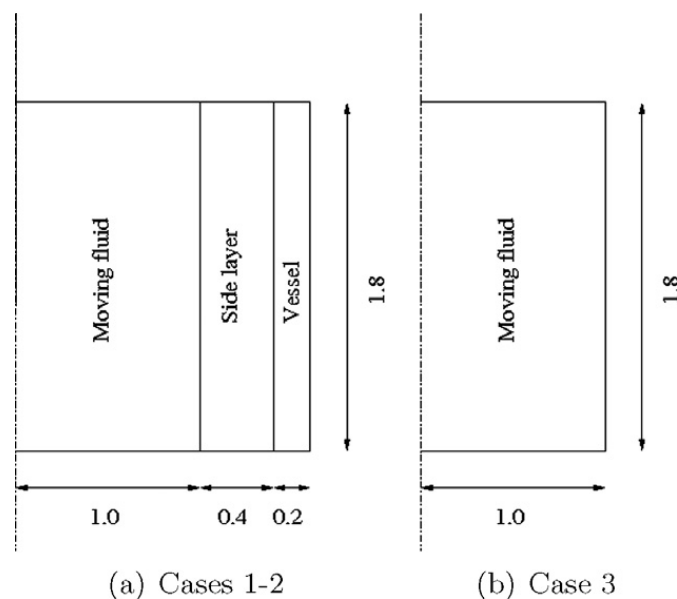


Fig. 8. Two simplified domains where the thickness of the copper envelope is zero.

azimuthal modes of \mathbf{H}^c . It is also known that the Fourier mode $m = 1$ is the most unstable one [28,24,29,18]; therefore, we investigate only this mode. We denote $\mathbf{H}^c(m = 1)$ the Fourier mode $m = 1$ of \mathbf{H}^c .

The above three problems are solved by advancing 3.11 in time using a small random divergence-free magnetic field as initial data. The magnetic energy of $\mathbf{H}^c(m = 1)$, $\frac{1}{2} \int_{\Omega^{2D}} \|\mathbf{H}^c(m = 1)\|^2 dx$, is recorded as a function of time for various magnetic Reynolds numbers $R_m \in [25, 100]$. The critical magnetic Reynolds number R_{mc} corresponds to zero growth rate. The critical magnetic Reynolds numbers for the three cases defined above are reported in Table 6. By comparing cases 1 and 2, we observe that the critical magnetic Reynolds number decreases when the VTF condition is used to model the soft iron impellers, thereby confirming that using soft iron impellers may indeed help to lower the dynamo threshold in the VKS2 experiment. The results of the third experiment (Case 3) show that using an envelope made of soft iron to confine the magnetic field within the 'bulk flow' region is counter-productive. Another interpretation of this result is that the presence of the 'side layer' may help the dynamo effect in the VKS2 experiment.

5.3. More realistic models

We now model the VKS2 experiment with more realistic geometries, electric conductivities, and magnetic permeabilities (see Fig. 7).

The conducting domain is partitioned into a moving region (comprising the 'bulk flow', 'lid flows', and the 'disk flows') and a stationary region (comprising the 'side layer' and the copper vessel), see Fig. 9.

The moving fluid region is $(r, z) \in [0, R_0] \times [-1.275, 1.275]$ and the stagnant sodium 'side layer' is $r \in [R_0, R_1]$, $R_1 = 1.4 R_0$. The moving fluid region is divided into the 'bulk flow' subregion $(r, z) \in [0, R_0] \times [-0.9, 0.9]$, the 'disk flows' subregions $(r, z) \in [0, R_0] \times [-0.975, -0.9] \cup [0.9, 0.975]$, and the 'lid flows' subregions $(r, z) \in [0, R_0] \times ([-1.275, -0.975] \cup [0.975, 1.275])$. The purpose of the 'disk flows' is to model the two impellers and the fluid moving between the blades. To account for the presence of solids of various material properties in the 'disk flows' subregions, we also introduce two 'flat disks' of width $H_i = 0.075R_0$, radius $R_i = 0.75R_0$ and round edges.

The copper walls of the device are $(r, z) \in [R_1, R_2] \times [-1.475, 1.475]$, $R_2 = 1.6R_0$. Other geometrical dimensions are reported in Fig. 7.

The fluid is assigned the conductivity of liquid sodium σ_0 , ($\sigma_1 = \sigma_0$). The outer wall of the device is assigned the conductivity of copper, $\sigma_2 = 4.5\sigma_0$. The magnetic permeability of every component of the device is equal to that of the vacuum μ_0 except for the two 'flat disks'. Two different material compositions are tested for the 'flat disks'. In what we hereafter refer to as Case 1' and Case 2' the 'flat disks' are made of stainless steel, $\sigma_i = 0.14\sigma_0$ and $\mu_i = \mu_0$, but in Case 3' and Case 4' the 'flat disks' are made of soft iron, $\sigma_i = \sigma_0$ and $\mu_i = 60\mu_0$.

Table 6
Critical magnetic Reynolds number for Cases 1 to 3.

Case	Boundary condition	R_{mc}
1	Vacuum transmission condition	45
2	VTF at $z = \pm \frac{1}{2}H_0$, $0 \leq r \leq R_0$	40
3	VTF everywhere	52

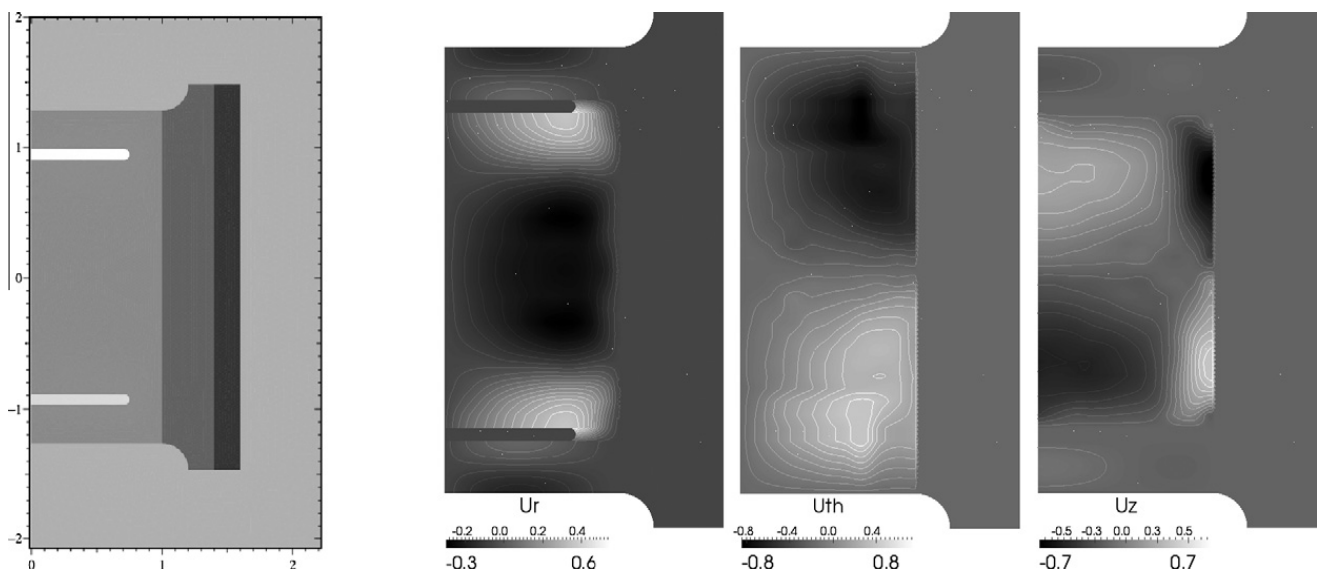


Fig. 9. Simplified VKS2 setting and imposed axisymmetric velocity field $\bar{\mathbf{u}}$ for Case 2' and Case 4'.

The prescribed axisymmetric velocity field \mathbf{u} is defined separately in the 'bulk flow', 'disk flow', and 'lid flow' regions. In the 'bulk flow' region \mathbf{u} is modeled as in the previous section by using the axisymmetric time-averaged flow field measured in a water experiment which is documented in [28]. The flow is interpolated on the finite element grid and normalized by the maximum of the Euclidian norm of the velocity, U_{\max} . The quantity U_{\max} is chosen to be the reference velocity scale, $U := U_{\max}$. Let us denote by $u_0(r,z)\mathbf{e}_\theta$ the axisymmetric 'bulk flow'. Then the flow in the top 'disk flow' region is defined to be equal to $u_0(r,0.9)\mathbf{e}_\theta$ and the flow in the bottom 'disk flow' region is defined to be equal to $u_0(r,-0.9)\mathbf{e}_\theta$. Finally, two different models are tested for the 'lid flow'. In the first model the top 'lid flow' velocity field is defined to be the linear interpolation with respect to z between $u_0(r,0.9)\mathbf{e}_\theta$ and the zero, and the bottom flow is defined similarly. The 'lid flow' thus defined is denoted $\mathbf{u}_\theta^{\text{lin}}$. In the second model the 'lid flow' velocity is defined to be the sum of $\mathbf{u}_\theta^{\text{lin}}$ and 10% of an analytical poloidal recirculation flow \mathbf{u}^{pol} that has been introduced in [24]. The flow \mathbf{u}^{pol} is normalized so that the maximum of Cartesian norm of \mathbf{u}^{pol} is U_{\max} .

We use $\mathbf{u}_\theta^{\text{lin}}$ in the 'lid flow' region in Case 1' and Case 3', and we use $\mathbf{u}_\theta^{\text{lin}} + 10^{-1}\mathbf{u}^{\text{pol}}$ in the 'lid flow' region in Case 2' and Case 4'. The three components of the velocity field \mathbf{u} which is used in Case 2' and Case 4' are shown in Fig. 9. The velocity has a continuous azimuthal component and shows a small recirculation in the 'lid flow' region.

The critical magnetic Reynolds numbers are computed in the four cases defined above by solving 3.11 for various Reynolds numbers and evaluating the growth rate of the magnetic energy in each case. The critical magnetic Reynolds number R_{mc} corresponds to zero growth rate. The results are reported in Table 7.

When comparing Case 1 from Table 6 with Case 1' from Table 7, one realizes that adding counter-rotating disks (modeled by the 'disk flows') and purely azimuthal 'lid flows' dramatically increases the dynamo thresholds; R_{mc} goes from 45 to 82. The adverse effect of the 'lid flows' was first demonstrated in [29]. Adding a poloidal component to the 'lid flow' with 10% recirculation intensity (Case 2') lowers the threshold from 82 to 75 which is still larger than 45. Hence, changing the

Table 7
Critical magnetic Reynolds number for the Fourier mode $m=1$ in VKS2 simplified setting.

Case	Composition of disk	Lid flow	R_{mc}
1'	Stainless steel	$\mathbf{u}_\theta^{\text{lin}}$	82
2'	Stainless steel	$\mathbf{u}_\theta^{\text{lin}} + 10^{-1}\mathbf{u}^{\text{pol}}$	75
3'	Soft iron	$\mathbf{u}_\theta^{\text{lin}}$	66
4'	Soft iron	$\mathbf{u}_\theta^{\text{lin}} + 10^{-1}\mathbf{u}^{\text{pol}}$	64

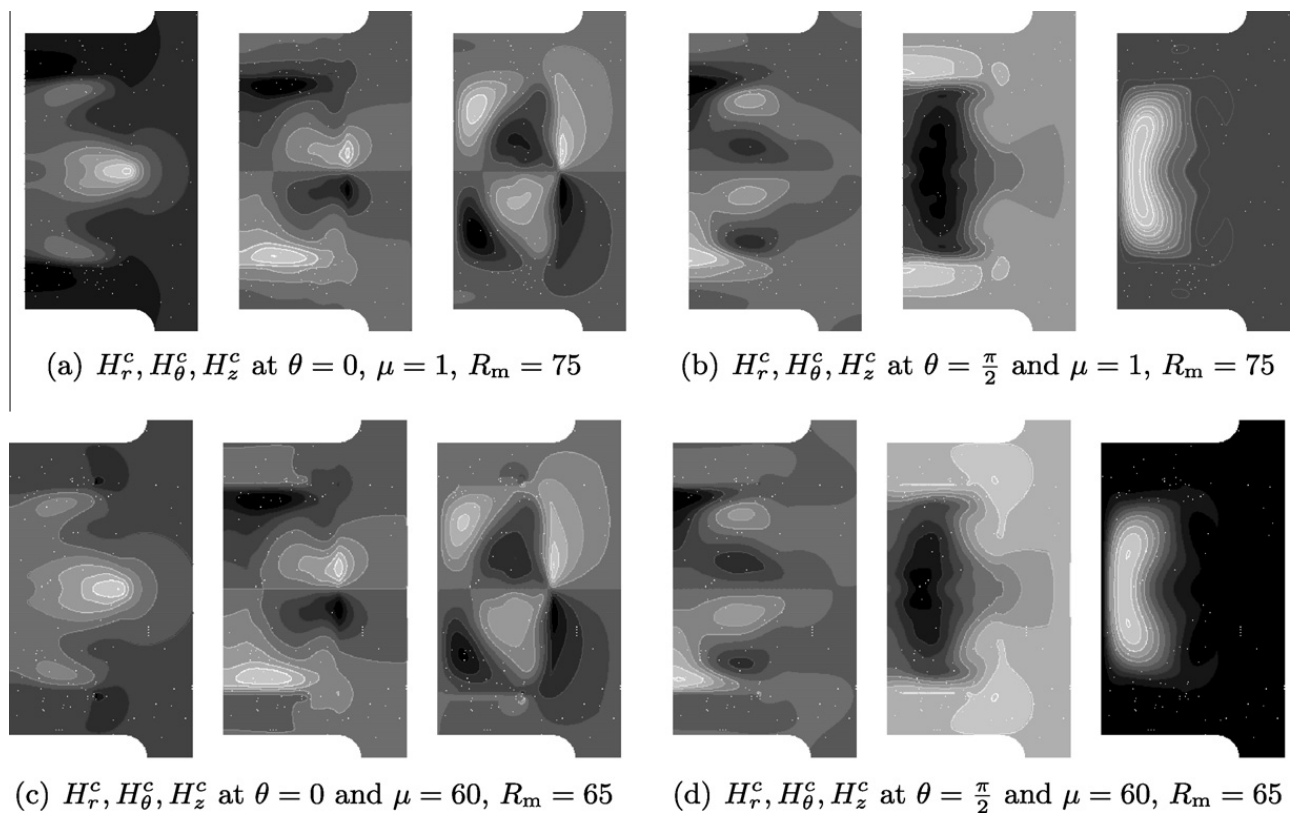


Fig. 10. Magnetic field in two perpendicular azimuthal planes in Cases 2' and 4'.

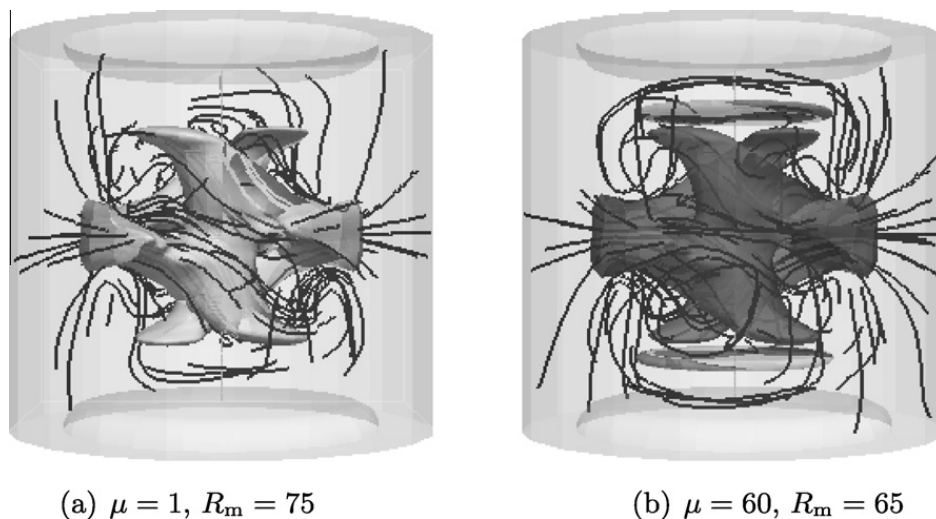


Fig. 11. Magnetic lines and iso-value of the magnetic energy density corresponding to 25% of the maximum magnetic energy for Cases 2' and 4'.

magnetic permeability has more effect than tweaking the 'lid flow'. The threshold goes further down to $R_{mc} = 65 \pm 1$ in both Cases 3' and 4'.

We show in Fig. 10 the two unstable modes of the magnetic field corresponding to Cases 2' and 4'. They look similar in the 'bulk flow' region. There is an equatorial dipole and two vertical structures of opposite sign. Noticeable differences become apparent when observing the magnetic lines close to the counter-rotating disks as shown in Fig. 11.

The general conclusion of this parametric study is that ferromagnetic disks have a measurable impact on the dynamo threshold, which is crucial since the experimental magnetic Reynolds number is constrained to be below 50 in the VKS2 experiment. A provisional result about ferromagnetic disks is that they may screen the 'bulk flow' from the influence of the 'lid flow', thereby lowering the dynamo threshold for the Fourier mode $m = 1$ of the magnetic field. These numerical experiments also confirm the importance of moving soft iron material in the VKS2 dynamo. This may be one piece of the big maze that constitutes the VKS2 experiment, but more experimental and numerical investigations need to be done to fully understand this experiment. This illustrates clearly the unending interplay between MHD experiments and simulations.

6. Conclusion

We have developed a novel approximation technique using Lagrange finite elements for solving magneto-dynamics problems involving discontinuous magnetic permeability and non-smooth interfaces. The method has been applied to model the VKS2 experiment in a kinematic dynamo context. In the future, we will investigate nonlinear regimes with the full MHD equations in a VKS2 set-up using impellers modeled by flat disks together with an axisymmetric volume forcing term acting at the location of the blades.

Acknowledgments

This work was granted access to the HPC resources of IDRIS under the allocation 2010- [0254] made by GENCI (Grand Equipement National de Calcul Intensif). J.L.G. is thankful to University Paris Sud 11 for supporting him in June 2009, January 2010, and January 2011. F.L. is thankful to Texas A& M University for supporting him in 2010/2011.

References

- [1] A. Alonso, A mathematical justification of the low-frequency heterogeneous time-harmonic Maxwell equations, *Math. Models Methods Appl. Sci.* 9 (3) (1999) 475–489.
- [2] D.N. Arnold, An interior penalty finite element method with discontinuous elements, *SIAM J. Numer. Anal.* 19 (1982) 742–760.
- [3] G.A. Baker, Finite element methods for elliptic equations using nonconforming elements, *Math. Comp.* 31 (137) (1977) 45–59.
- [4] A. Bonito, J.-L. Guermond, Approximation of the eigenvalue problem for the time harmonic Maxwell system by continuous Lagrange finite elements, *Math. Comp.* (2011), doi:10.1090/S0025-5718-2011-02464-6.
- [5] A. Bossavit, *Computational electromagnetism, variational formulations, complementary*, *Edge Elem. Electromagnet.*, vol. 2, Academic Press, New York, NY, 1998.
- [6] H. Brezis *Analyse fonctionnelle, Théorie et applications*. [Functional Analysis. Theory and applications], Applied Mathematics Series for the Master's Degree, Masson, Paris, France, 1983.
- [7] M. Costabel, A coercive bilinear form for Maxwell's equations, *J. Math. Anal. Appl.* 157 (2) (1991) 527–541.
- [8] T.G. Cowling, The magnetic field of sunspots, *Mon. Not. Roy. Astr. Soc.* 94 (1934) 39–48.
- [9] M. Dauge, Benchmark for Maxwell, 2009. (<<http://perso.univ-rennes1.fr/monique.dauge/benchmax.html>>).
- [10] E. Durand, *Magnétostatique*, Masson, Paris, 1968.

- [11] A. Gaillitis, O. Lielausis, S. Dement'ev, E. Platacis, A. Cifersons, Detection of a flow induced magnetic field eigenmode in the Riga dynamo facility, *Phys. Rev. Lett.* 84 (2000) 4365.
- [12] A. Giesecke, C. Nore, F. Plunian, R. Laguerre, A. Ribeiro, F. Stefani, G. Gerbeth, J. Léorat, J.-L. Guermond, Generation of axisymmetric modes in cylindrical kinematic mean-field dynamos of VKS type, *Geophys. Astrophys. Fluid Dyn.* 104 (2) (2010) 249–271.
- [13] A. Giesecke, C. Nore, F. Stefani, G. Gerbeth, J. Léorat, F. Luddens, J.-L. Guermond, Electromagnetic induction in non-uniform domains, *Geophys. Astrophys. Fluid Dyn.* 104 (5–6) (2010) 505–529.
- [14] C. Gissinger, S. Fauve, E. Dormy, Bypassing Cowling's theorem in axisymmetric fluid dynamos, *Phys. Rev. Lett.* 101 (2008). 144502.
- [15] J.-L. Guermond, R. Laguerre, J. Léorat, C. Nore, An interior penalty Galerkin method for the MHD equations in heterogeneous domains, *J. Comput. Phys.* 221 (1) (2007) 349–369.
- [16] J.-L. Guermond, R. Laguerre, J. Léorat, C. Nore, Nonlinear magnetohydrodynamics in axisymmetric heterogeneous domains using a Fourier/finite element technique and an interior penalty method, *J. Comput. Phys.* 228 (8) (2009) 2739–2757.
- [17] A. Herzenberg, F.J. Lowes, Electromagnetic induction in rotating conductors, *Phil. Trans. Roy. Soc. London, Series A, Math. Phys. Sci.* 249 (970) (1957) 507–584.
- [18] R. Laguerre. Approximation des équations de la MHD par une méthode hybride spectrale-éléments finis nodaux : application à l'effet dynamo. Ph.D. thesis, University of Paris VII, 2006.
- [19] R. Laguerre, C. Nore, A. Ribeiro, J. Léorat, J.-L. Guermond, F. Plunian, Impact of impellers on the axisymmetric magnetic mode in the VKS2 dynamo experiment, *Phys. Rev. Lett.* 101 (10) (2008). 104501.
- [20] R.B. Lehoucq, D.C. Sorensen, C. Yang, *ARPACK users' guide of Software, Environments and Tools*, Society for Industrial and Applied Mathematics (SIAM), Philadelphia, PA, 1998. Solution of large-scale eigenvalue problems with implicitly restarted Arnoldi methods.
- [21] J. Léorat, C. Nore, Interplay between experimental and numerical approaches in the fluid dynamo problem, *Comptes Rendus Physique* 9 (2008) 741–748.
- [22] J.-L. Lions, E. Magenes, *Problèmes aux Limites non Homogènes et Applications*, 1, Dunod, Paris, France, 1968.
- [23] L. Marié, J. Burguete, F. Daviaud, J. Léorat, Numerical study of homogeneous dynamo based on experimental von Kármán type flows, *Eur. Phys. J. B* 33 (2003) 469–485.
- [24] L. Marié, C. Normand, F. Daviaud, Galerkin analysis of kinematic dynamos in the von Kármán geometry, *Phys. Fluids* 18 (2006). 017102.
- [25] R. Monchaux, M. Berhanu, S. Aumaitre, A. Chiffaudel, F. Daviaud, B. Dubrulle, F. Ravelet, S. Fauve, N. Mordant, F. Pétrélis, M. Bourgoin, Ph. Odier, J.-F. Pinton, N. Plihon, R. Volk, The von Kármán sodium experiment: Turbulent dynamical dynamos, *Phys. Fluids* 21 (2009). 035108.
- [26] R. Monchaux, M. Berhanu, M. Bourgoin, Ph. Odier, M. Moulin, J.-F. Pinton, R. Volk, S. Fauve, N. Mordant, F. Pétrélis, A. Chiffaudel, F. Daviaud, B. Dubrulle, C. Gasquet, L. Marié, F. Ravelet, Generation of magnetic field by a turbulent flow of liquid sodium, *Phys. Rev. Lett.* 98 (2007). 044502.
- [27] F. Pétrélis, N. Mordant, S. Fauve, On the magnetic fields generated by experimental dynamos, *Geophys. Astrophys. Fluid Dyn.* 101 (2007) 289.
- [28] F. Ravelet, A. Chiffaudel, F. Daviaud, J. Léorat, Towards an experimental von Kármán dynamo: numerical studies for an optimized design, *Phys. Fluids* 17 (2005) 117104.
- [29] F. Stefani, M. Xu, G. Gerbeth, F. Ravelet, A. Chiffaudel, F. Daviaud, J. Léorat, Ambivalent effects of added layers on steady kinematic dynamos in cylindrical geometry: application to the VKS experiment, *Eur. J. Fluid Mech. B* 25 (2006) 894.
- [30] R. Stieglitz, U. Müller, Experimental demonstration of a homogeneous two-scale dynamo, *Phys. Fluids* 13 (2001) 561.
- [31] L. Martin Witkowski, P. Marty, J.S. Walker, Multidomain analytical-numerical solution for a rotating magnetic field with finite-length conducting cylinder, *IEEE Trans. Magnet.* 36 (2000) 452–460.